

1 **Measurement report: Hygroscopicity of Size-Selective Aerosol
2 Particles at Heavily Polluted Urban Atmosphere of Delhi:
3 Impacts of Chloride Aerosol**

4 Anil Kumar Mandariya^{1,2}, Ajit Ahlawat³, Mohd. M. V. Haneef¹, Nisar A. Baig¹, Kanan
5 Patel⁴, Joshua S. Apte⁵, Lea Hildebrandt Ruiz⁴, Alfred Wiedensohler^{3*}, and Gazala Habib^{1*}

6 ¹Department of Civil Engineering, Indian Institute of Technology Delhi, New Delhi, India

7 ²now at: Univ Paris Est Creteil and University Paris Cité, CNRS, LISA, F – 94010 Créteil, France

8 ³Leibniz Institute for Tropospheric Research (TROPOS), Permoserstraße, 15 Leipzig, Germany

9 ⁴Department of Civil, Architectural and Environmental Engineering, The University of Texas at Austin, Austin,
10 Texas, USA

11 ⁵McKetta Department of Chemical Engineering, The University of Texas at Austin, Austin, Texas, USA

12 *Correspondence to:* Gazala Habib (gazalahabib@civil.iitd.ac.in) and Alfred Wiedensohler (ali@tropos.de)

13 **Abstract.** Recent research has unveiled the pivotal role of wintertime episodic high chloride emissions in the
14 Delhi region, which significantly influence aerosol hygroscopicity and aerosol-bound liquid water, thereby
15 contributing to the initiation of fog episodes in Delhi. However, these findings have primarily relied on modeled
16 aerosol hygroscopicity, necessitating validation through direct hygroscopicity measurements. In this study, we
17 present the measurement results of bulk aerosol composition of non-refractory PM₁ from ACSM and size-resolved
18 (Nucleation, Aitken, and Accumulated mode particles) hygroscopic growth factor and associated hygroscopicity
19 parameter at 90% relative humidity (RH) measured using H-TDMA (Hygroscopic-Tandem Differential Mobility
20 Analyser) at Delhi Aerosol Supersite (DAS) for the first time. Our observations indicate that the hygroscopicity
21 parameter ($\kappa_{H-TDMA_90\%}$) ranges from 0.00 to 0.11 (with an average of 0.03 ± 0.02) for 20 nm aerosol particles,
22 0.05 to 0.22 (0.11 ± 0.03) for 50 nm particles, 0.05 to 0.30 (0.14 ± 0.04) for 100 nm particles, 0.05 to 0.41 (0.18 ± 0.06) for 150 nm particles, and 0.05 to 0.56 (0.22 ± 0.07) for 200 nm particles. Remarkably, our results reveal
23 that the period characterized by high chloride (H-Cl) emissions exhibits significantly higher hygroscopicity (0.35 ± 0.06) compared to periods marked by high biomass burning (H-BB) (0.18 ± 0.04), high hydrocarbon-like
24 organic aerosol (H-HOA) (0.17 ± 0.05), and relatively cleaner periods (0.27 ± 0.07). This study provides first
25 observational evidence of Ammonium Chloride as the major contributor to aerosol hygroscopic growth and liquid
26 water content in Delhi, which highlights the role of Ammonium Chloride in aerosol-water interaction and related
27 haze/fog development. Additionally, the high chloride content in aerosols appears to counteract the negative
28 effects of high organic aerosol (OA) levels on cloud condensation nuclei (CCN) activity.
29
30
31
32

33 **1. Introduction**

34 The Intergovernmental Panel on Climate Change (IPCC) reported that aerosol-cloud interaction is still not fully
35 understood and has significant uncertainties in quantifying global radiative budgets. Aerosol hygroscopicity plays
36 a pivotal role in overcoming and explaining these uncertainties. Hygroscopicity is crucial to understand how the
37 aerosol particles act as cloud condensation nuclei (CCN) and forms fog droplets/haze at sub-saturated/nearly
38 saturation and cloud droplets at atmospheric supersaturation levels (McFiggans et al., 2006; Topping and
39 McFiggans, 2012). Its understanding is crucial to predict the aerosol size distribution and scattering properties
40 better in global models under varying atmospheric humidity (RH) conditions (Randall et al., 2007).
41 Hygroscopicity at higher RH atmospheric conditions leads to an enhanced aerosol cross-sectional area, resulting
42 in efficient light scattering by the aerosol particles (Tang and Munkelwitz, 1994). It mainly depends on particle
43 size and chemical composition. Generally, the inorganic salts such as ammonium salts of sulfate, nitrate, and
44 chloride, are highly hygroscopic (Hu et al., 2011; Petters and Kreidenweis, 2007), organic aerosol (OA) are
45 comparatively less hygroscopic (Jimenez et al., 2009; Kroll et al., 2011), while dust particles and black/elemental
46 carbon particles are stated as hydrophobic (Seinfeld and Pandis, 2006). Further, the elevated atmospheric RH
47 during winter and monsoon favour the formation of more oxidized secondary organic aerosol (SOA) via aqueous-
48 phase (Ervens et al., 2011) and heterogeneous reactions (McNeill, 2015), leads to enhancement in organic aerosol
49 hygroscopicity (Jimenez et al., 2009; Mei et al., 2013) which adversely impact on the local visibility (Li et al.,
50 2016; Liu et al., 2012). However, aerosol loading inversely affects aerosol hygroscopicity (Mandariya et al.,
51 2020a). Apart from it, aerosol loading is also a critical factor in deciding the lifetime of cloud, which affects the
52 region's rain quantitatively (Albrecht, 1989; Lohmann and Feichter, 2005).

53 Over the past decades, aerosol hygroscopicity has been intensively measured using hygroscopic tandem
54 differential mobility analyzer (H-TDMA) (Massling et al., 2005; Gysel et al., 2007; Mandariya et al., 2020;
55 Swietlicki et al., 2008; Yeung et al., 2014; Kecorius et al., 2019) and CCN (Bhattu and Tripathi, 2015; Gunthe et
56 al., 2011; Massoli et al., 2010; Ogawa et al., 2016) counter under sub- and supersaturation levels, respectively.
57 Petters and Kreidenweis (2007) introduced a hygroscopicity parameter, kappa (κ), to associate aerosol
58 hygroscopicity with its chemical composition. Furthermore, hygroscopicity associated with OA potentially varies
59 with OA chemical properties like solubility, the extent of dissociation in aerosol water, and surface activity
60 (Hallquist et al., 2009; Jimenez et al., 2009), leads to difficulty in the quantification of OA hygroscopicity, result
61 in introducing more discrepancies in predicted and measured aerosol hygroscopicity. Hence, there is a need to

62 explore measurement-based aerosol hygroscopicity for Delhi's atmosphere to understand the frequent haze/cloud
63 formations better.

64 In past decades, fast economic growth and industrialization in the Indo Gangetic Plain (IGP) led to severe air
65 quality during wintertime (Wester et al., 2019). Delhi is potentially affected by local and regional air pollution
66 problems in wintertime (Arub et al., 2020; Bhandari et al., 2020; Gani et al., 2019; Prakash et al., 2018). Recent
67 studies (Gani et al., 2019; Rai et al., 2020) have shown chloride is one of the predominant factors to degrade the
68 air quality in the Delhi region and significantly favour the haze/fog formation during winter (Gunthe et al., 2021).
69 Trash and biomass burning for heating and waste degradation are among the main contributors to chloride in Delhi
70 (Rai et al., 2020). A recent study conducted in Delhi reported that frequent high chloride events promotes high
71 aerosol liquid water content under elevated humid condition leads to haze and poor visibility in the city (Chen et
72 al., 2022). In addition, Gunthe et al. (2021) showed higher chloride also facilitates enhancement in aerosol
73 hygroscopicity, however, this study was based on theoretical hygroscopicity. Therefore, it is essential to investigate
74 the impacts of chloride on aerosol hygroscopicity and its potential to enhance aerosol-bound liquid water based
75 on field measurements. Moreover, the hygroscopicity of the aerosol particles in the heavily polluted urban
76 atmosphere, which confines to highly complex composition, is extremely limited, like Delhi, situated at Indo
77 Gangetic Plain (IGP), India, where air quality severely degrades during haze/fog-dominated. To the author's best
78 knowledge, the current study is first in Delhi, India, exploring a complex atmosphere of IGP using H-TDMA-
79 measured aerosol hygroscopicity. Hence, it is essential to measure size-resolved aerosol hygroscopicity in Delhi's
80 atmosphere and investigate its role in the context of high chloride.

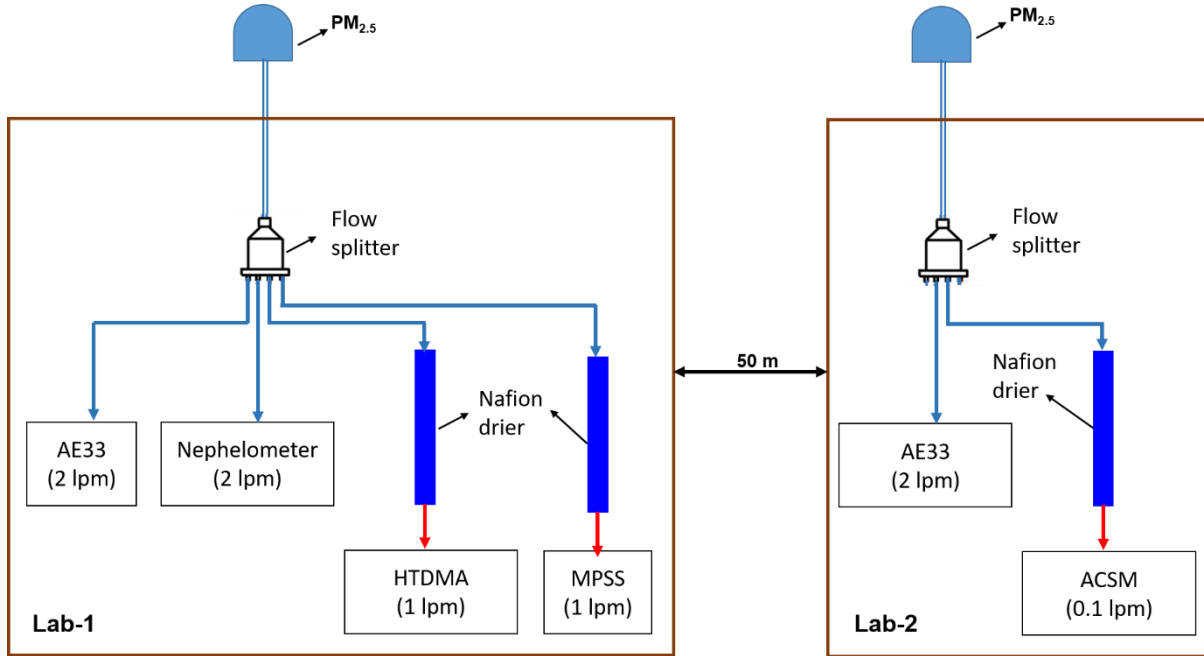
81 **2. Experimental Methods**

82 **2.1 Aerosol Measurements**

83 Real-time atmospheric aerosol measurements were conducted simultaneously using Hygroscopic-Tandem
84 Differential Mobility Analyzer (H-TDMA), Mobility Particle Size Spectrometer (MPSS), and Aerodyne Aerosol
85 Chemical Speciation Monitor (ACSM, Aerodyne Research, Billerica MA) during winter (1st February 2020 to
86 16th March 2020) at the Indian Institute of Technology (IIT) Delhi in Block 5, at the height of nearly 15 m above
87 ground level (a.g.l.) as shown in Fig. 1. The lab-2 is situated at the height of 15 m a.g.l. and lab-2 is 50 m apart
88 from lab-1.

89 In this study, the HTDMA system was used to investigate the hygroscopic growth of size-resolved particles at 90
90 % RH. The HTDMA system has been previously used in many field campaigns (Massling et al., 2007; Wu et al.,

91 2013b; Zhang et al., 2016). The HTDMA system (TROPOS, Germany) is comprised of two Differential Mobility
92 Analyzers (DMAs, type Hauke-median, TROPOS, Germany), a Condensation Particle Counter (CPC, Model
93 3772, TSI Inc., USA) along with a humidifier system located between the two DMAs. The role of first DMA is
94 to select the quasi-monodisperse particles at a dry diameter (D_p , dry) with 30% RH. After that, the size-selected
95 particles pass through a humidity conditioner, which can be adjusted from 30% to 90% RH by regulating the
96 aerosol and sheath air flow by mixing dry air with RH<5% and humid air with ~95% RH (Maßling et al., 2003).
97 The uncertainties associated with RH measurement at 90% RH is 1.0%. The particle hygroscopic growth
98 distribution at dry size (D_p , dry) at a certain humidity can be easily determined with CPC. There are two humidity
99 sensors (Vaisala) in the system for aerosol and sheath respectively. The humidity sensors positioned in the second
100 DMA were calibrated automatically with 100 nm ammonium sulfate ($(NH_4)_2SO_4$) particles every 30 min at 90%
101 RH to analyze the stability at high RH. The measurement error of the HTDMA mainly depends on the uncertainty
102 in measuring and controlling the RH within the system (Su et al., 2010). Therefore, all RH sensors were calibrated
103 using the Vaisala salt kit comprising LiCl, NaCl, KCl etc. prior the measurement campaign. Both the DMAs were
104 size calibrated by applying the Latex particles with the standard size of 200 nm before the start of the measurement.
105 The number concentration peak occurred at 203 nm, referring to accuracy of DMAs size selection at 1.5%.
106 HTDMA system was operated at 90% RH to measure the hygroscopic growth factors (HGFs) for particles with
107 D_p , dry of five different sizes i.e. 20, 50, 100, 150 and 200 nm. The time resolution of the full scan covering the
108 five sizes was about 30 min.
109 Particle number size distributions (PNSDs) and particle volume-size distributions (PVSDs) were measured using
110 a Mobility Particle Size Spectrometer (MPSS (TROPOS type)).
111 A Detailed description of ACSM setup can be found in Arub et al. (2020). ACSM was operated at nearly 0.1 lpm
112 at 1 min time resolution in a temperature-controlled laboratory. ACSM was set to run to measure mass-to-charge
113 ratio (m/z) m/z 10 to m/z 140. The ACSM measures non-refractory particulate matter less than 1 μ m (NR-PM₁).
114 The concentrate PM₁ aerosol beam was impacted on the vaporizer at 600 °C and flash-vaporized compounds were
115 subsequently ionized through impact ionization at 70 eV electron and detected with a quadrupole mass
116 spectrometer (Ng et al., 2011). The 200 ms amu⁻¹ scan speed and pause setting at 125 for a sampling time (64 s)
117 were set to acquire aerosol mass spectra in ACSM. Detailed operational procedures for the ACSM are explained
118 elsewhere in Gani et al. (2019).



119

120 **Figure 1: Schematic diagram of the inlet systems for aerosol sampling instruments. The blue and red**
 121 **sampling lines indicate the ambient air and dehumidified (RH<25%) ambient air, respectively.**

122 **2.2 Meteorological and Gas Data**

123 The gas data was taken from the location site R.K Puram -DPCC, a continuous ambient air quality monitoring
 124 station controlled by the central control room for air quality management (Delhi-NCR). The gas data were
 125 downloaded from the CPCB website (<https://app.cpcbccr.com/CCR/#/caaqm-dashboard/caaqm-landing/data>). R.K.
 126 Puram is located 3.5 km northwest of IIT Delhi. The wind speed (WS), wind direction (WD), temperature (T),
 127 and relative humidity (RH) were continuously measured using an automatic weather station (Watch Dog 2000
 128 series). The weather station is mounted over the top of the 9th-floor building of the IITD.

129 **2.3 Data Analysis**

130 **2.3.1 H-TDMA**

131 Overall, we recorded 1483 H-TDMA scans cycles. Afterward, the % difference between measured and theoretical
 132 growth factors (Δq) was calculated after each scan cycle for 100 nm ammonium sulfate particles. Those scan
 133 cycles came between $\Delta q \leq \pm 5\%$, were only carried out for further data treatment, and the rest scans cycles were
 134 discarded (Kecorius et al., 2019). Thus, we had 1102 H-TDMA scan cycles following this data quality check.
 135 Regarding good scan cycles, we had 1449, 1431, 1438, 1470, and 1420 good H-TDMA scans for 20, 50, 100,
 136 150, and 200 nm particles, respectively, to further analyze. Afterward that, a piecewise linear TDMAinv

137 algorithm, namely TDMAinv Toolkit, written in IgorPro and developed by Gysel et al. (2009), was used to do
138 post-data treatment on the raw HGF. Because the measured distribution function is a skewed and smoothed
139 integral transform of the actual growth factor probability density functions (GF-PDFs). A detailed description of
140 the raw data processing in the TDMAinv toolkit to measure real HGFs is described in Gysel et al. (2009). The
141 TDMAinv toolkit was successfully used in various studies around the globe (Gysel et al., 2007; Liu et al., 2012;
142 Sjogren et al., 2007; Wang et al., 2018a) and at Kanpur, India (Mandariya et al., 2020a). Besides, the RH in the
143 DMA2 generally achieved the set value of 90% and remained stable within $\pm 1\%$, although occasionally, it faced
144 a more considerable drift. All growth factors measured between 88 and 92% RH were corrected to a target value
145 of 90% (HGF_90%) (Gysel et al., 2007) using the kappa-model suggested in the TDMAinv toolkit (Gysel et al.,
146 2009) to minimize this DMA2 RH drifts. After it, 979, 957, 972, 969, and 966 scans were found corrected at target
147 RH for 20, 50, 100, 150, and 200 nm aerosol particles, respectively, which further averaged for 60 min time
148 resolution and finally, these numbers reached to 425, 429, 419, 424, and 417, respectively.

149 Further, size-resolved hygroscopicity factors (kappa, κ , say $\kappa_{H-TDMA_90\%}$) were calculated from the respective size-
150 resolved target RH corrected HGFs using equation (1) kappa-Köhler theory (Mandariya et al., 2020a; Petters and
151 Kreidenweis, 2007).

$$152 \quad \kappa_{H-TDMA_90\%} = (HGF_90\%^3 - 1) \left[\frac{1}{RH} \exp \left(\frac{4\sigma M_w}{RT \rho_w D_o HGF_{90\%}} \right) - 1 \right], \quad (1)$$

153 Where, $\kappa_{H-TDMA_90\%}$ is the hygroscopicity factor at 90% RH, HGF_90% is the size-resolve HGF at 90% RH, RH
154 is the atmospheric relative humidity in fraction, σ is the surface tension of the aerosol liquid droplet-air interface
155 at the droplet surface in N/m and can be assumed nearly to pure water, R is the universal gas constant in J K⁻¹ mol⁻¹,
156 M_w is the molecular mass of water, T is the ambient temperature in Kelvin (K), ρ_w is the density of water in
157 kg/m³, and D_o is the dry mobility diameter of the particle in m.

158 **2.3.2 MPSS**

159 MPSS measures electrical mobility distribution, which is then converted to PNSD in the 8 to ~ 800 nm mobility
160 diameter range by applying an inversion algorithm to correct for multiple charged aerosol particles (Wiedensohler,
161 1988; Pfieffer et al., 2014) and diffusional losses (Wiedensohler et al., 2012; 2018).

162

163

164 **2.3.3 ACSM**

165 An Aerodyne Aerosol Chemical Speciation Monitor (ACSM, Aerodyne Research, Billerica MA) provided mass
166 concentrations of organic aerosol (OA), ammonium (NH₄), sulfate (SO₄), nitrate (NO₃), and chloride (Cl). Details
167 on ACSM calibration and data processing are in Patel et al., 2021. We conducted Positive matrix factorization
168 (PMF) on the data and found a four-factor solution (hydrocarbon-like OA, “HOA”; biomass burning OA,
169 “BBOA”; less-oxidized OA, “LO-OOA”; more-oxidized OA “MO-OOA) to best represent the data set. Further
170 details about PMF analysis are in section S.1 of the SI. Furthermore, based on the mass concentration peaks of
171 BBOA, HOA, and Cl in the temporal variation (Fig. 1), respectively, three different events were characterized: 1)
172 High-residential or biomass burning (H-BB), 2) High-hydrocarbon-like OA (H-HOA), and 3) High-chloride (H-
173 Cl) period. In addition, the “Clean Period” was defined where PM₁ loading was less than 25 percentiles (≤ 38.7
174 $\mu\text{g m}^{-3}$) of the sampling period. The starting and end time of the event was defined by the starting the increment
175 in the concentration and reaching the starting value while the concentration decreased.

176 **2.3.4 Derived Secondary Inorganic Salts**

177 The ACSM mainly measures OA, NO₃, SO₄, NH₄, and Cl. Therefore, we adopted a simplified ion-pairing scheme
178 reported by Gysel et al. (2007). However, Gysel et al. (2007) did not include NH₄Cl in their ion-pairing scheme;
179 therefore, we elaborated this scheme and made some modifications in this scheme to include ammonium chloride
180 (ACl) in the calculation. Hence, our modified ion-pairing scheme includes NH₄Cl (ACl), NH₄NO₃ (AN),
181 (NH₄)₂SO₄ (AS), NH₄HSO₄ (ABS), and H₂SO₄ (SA) are shown below:

182 **Case-1 R_{SO_4} (NH_4 to SO_4) ≤ 1**

183 $SA = 98.0795 \times \max(0, (n_S - n_A))$

184 $ABS = 115.11 \times n_A$

185 $AS = 0$

186 $AN = 0$

187 $ACl = 0$

188 **Case-2 $1 < R_{SO_4} < 2$**

189 SA = 0

190 ABS = $115.11 \times ((2 \times n_S) - n_A)$

191 AS = $132.1405 \times (n_S - n_A)$

192 AN = 0

193 ACl = 0

194 **Case-3 $R_{SO_4} \geq 2$**

195 SA = 0

196 ABS = 0

197 AS = $132.1405 \times n_S$

198 AN = $\left(\min \left(\left(n_A - \left(\frac{ABS}{115.11} \right) - \left(\frac{2 \times AS}{132.1405} \right) \right), n_N \right) \right) \times 80.0434$

199 ACl = $\left(\min \left(n_C, \left(n_A - \left(\frac{ABS}{115.11} \right) - \left(\frac{2 \times AS}{132.1405} \right) - \left(\frac{AN}{80.0434} \right) \right) \right) \right) \times 53.54$

200 Here, n denotes the number of moles, whereas A, N, S, and C denotes the NH₄, NO₃, SO₄, and Cl species. We
201 also predicted these inorganic salts concentrations from the ISORROPIA v2.1 model using NH₄, SO₄, NO₃, and
202 Cl. We found a strong correlation and nearly unit slope (0.9999) between the calculated and modelled inorganic
203 salts as presented in Fig. S1, which strongly justifies the new ion-pairing scheme adopted in this study.

204 **2.3.5 Windrose and Potential Source Contribution Function (PSCF)**

205 The windrose plot was plotted by openair in R package (<http://www.r-project.org>, <http://www.openair-project.org>). The 48-hour back trajectory of air masses reaching Delhi super site (DSL) at 500 m above the ground
206 at every hour for the entire study period was estimated by an offline based Hybrid Single-Particle Lagrangian
207 Integrated Trajectory (HYSPLIT4) model developed by NOAA/Air Resources Laboratory (ARL) (Draxler and
208 Hess, 1997). The input meteorological data for back trajectories were taken from the Global Data Assimilation
209

210 System (GDAS 0.5 degree) archive maintained by ARL (<http://ready.arl.noaa.gov/archives.php>). Further,
211 utilizing these estimated back trajectories as input combined with the measured mass fraction of chemical species
212 of bulk aerosol, Potential Source Contribution Function (PSCF) analysis was carried out with the help of a tool
213 called Zefir (V 3.7) written in Igor Pro (WaveMetrics). Detail description regarding Zefir tool can be found
214 elsewhere (Petit et al., 2017). In addition, box plots reported in the subsequent section were also plotted with the
215 help of this tool. The aerosol liquid water content (ALWC) as a function of inorganic species mass concentration,
216 ambient temperature (T), and ambient relative humidity (RH), was calculated by ISORROPIA-II model
217 (Fountoukis and Nenes, 2007).

218 **3. Result and Discussions**

219 **3.1 Overview of meteorology, trace gases, and aerosol characterization**

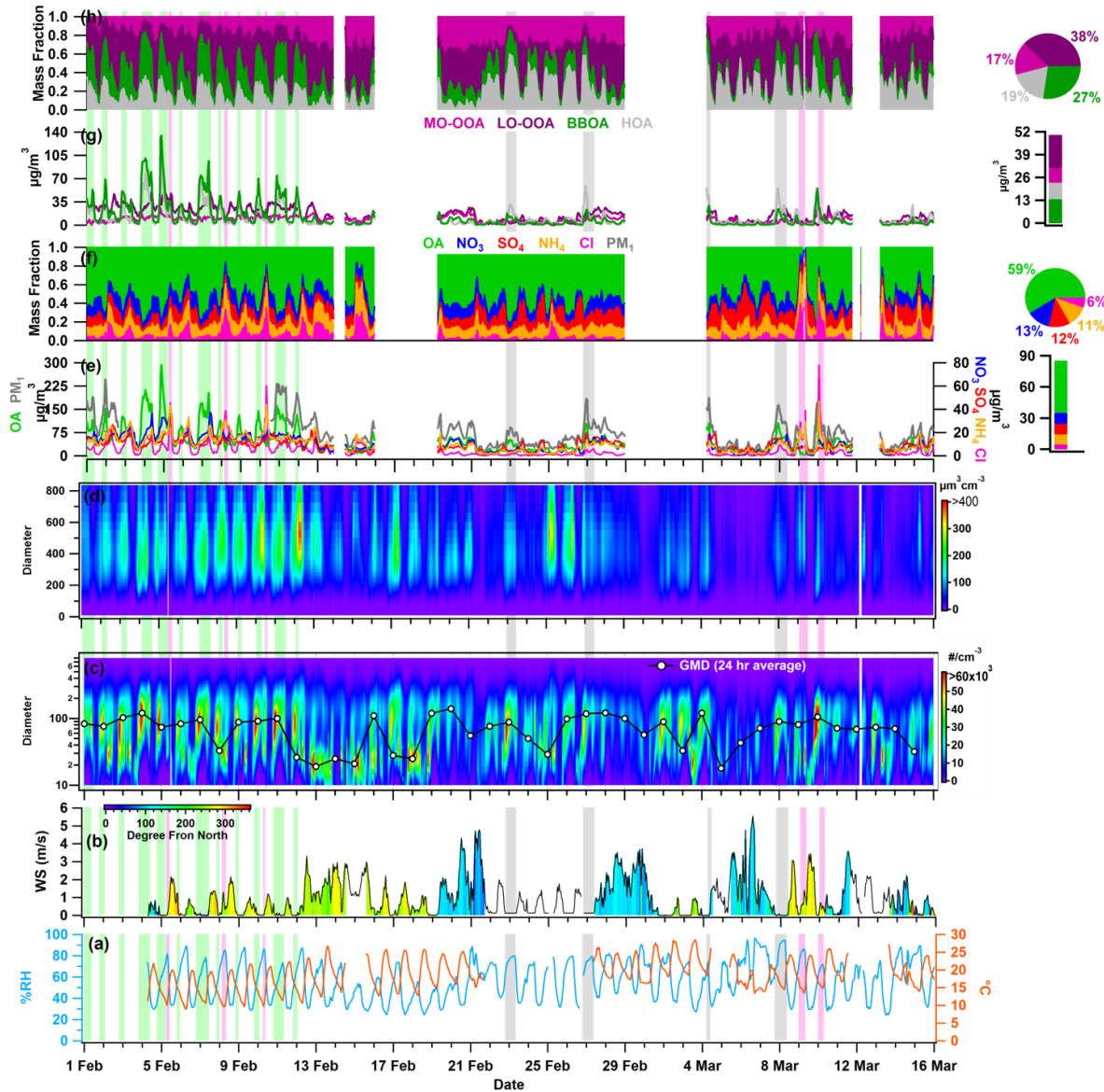
220 Fig. 2 illustrates the hourly-resolved temporal variability of meteorological parameters, including relative
221 humidity (RH), temperature (T), wind direction (WD), and wind speed (WS), as well as the particle number size
222 distribution (PNSD), particle volume size distribution (PVSD), principal components in non-refractory PM₁, and
223 organic aerosol (OA) with their fractional mass contributions. Additionally, Fig. S5 displays the temporal
224 variability of atmospheric gases, such as nitrogen oxides (NO_x), carbon monoxide (CO), and sulfur dioxide (SO₂).
225 Delhi's winter climate is primarily influenced by a depression generated by Western Disturbances, resulting in
226 cold waves in the region. The ambient relative humidity (RH) and temperature (T) exhibit variability in the range
227 of 24.2% to 96.6% and 9.0 °C to 28.5 °C, respectively, with average values of $56.0\% \pm 18.2\%$ and $18.7\text{ }^{\circ}\text{C} \pm 4.2\text{ }^{\circ}\text{C}$.
228 These fluctuations indicate that Delhi's atmosphere transitions from being wet and cold in February to dry and
229 relatively warm in March. Notably, nighttime conditions tend to be cooler and more humid compared to daytime
230 throughout the sampling period. Ambient RH exhibits a diurnal pattern, with a peak in the early morning (06:00-
231 07:00 hours) and a valley around midday (13:00-15:00 hours). In contrast, ambient temperature follows an
232 opposing trend, rising during midday, which can be correlated with higher solar radiation during those hours (see
233 Fig. 3a & b). The higher ambient temperature and peak O₃ concentration during midday (Fig. 3(i)) suggest the
234 presence of daytime photo-oxidation processes (Nelson et al., 2023). The wind speed (WS) and wind direction
235 (WD) varied from 0.0 to 5.6 (1.0 ± 1.0) m/s and 4.0 to 345.7 (197.1 ± 84.4) degrees from the North, respectively,
236 as shown in Fig. S6. Predominant wind directions were WNW-WSW and E-ESE. These patterns suggest that the
237 atmosphere remains relatively stagnant during the study period, and the measured aerosols likely represent
238 emissions and local aerosol chemistry in Delhi.

239 Additionally, ambient trace gases NO_x and CO exhibit significant variability throughout the sampling period,
240 peaking during local burning activities. Ambient NO_x levels reach a maximum of 421.2 ppb (58.4 ± 61.9) during
241 intense biomass burning activities. CO concentrations also peak during similar periods as NO_x and vary from 0.0
242 to 7.66 ppm (0.58 ± 0.79), as shown in Fig. S5. The diurnal variation of these trace gases is presented in Fig. 3 (f,
243 g, h, and i), with two peaks (06:00-08:00 and 17:00-20:00 hours) associated with morning local biomass/trash
244 burning emissions and nighttime traffic rush hours. In contrast, SO₂ follows a different trend, with dynamic
245 variations ranging from 0.46 to 9.55 ppb (4.41 ± 1.20) and showing peaks in the morning (09:00-12:00 hours) and
246 at midnight (21:00-02:00 hours) associated with the local industrial stack emissions.

247 The PM₁ particle number concentration ranges from 408 to 29,845 /cm³ (11319 ± 5552). High particle number
248 concentrations are typically associated with local burning events. The particle concentration increases in the
249 evening (at 18:00 hours) and reaches its maximum value at midnight, suggesting the resumption of residential
250 burning activity and traffic emissions. These activities likely contribute to the lower geometric mean diameter
251 (GMD) of the particle number size distribution (PNSD, approximately 47 nm), which increases to nearly 87 nm,
252 as shown in Fig. 3(t), indicating nighttime aging of organic aerosol. The hourly averaged mean diurnal GMD of
253 PVSD varies from approximately 274 to 324 nm (Fig. 3(y)), with a mean value of 309.1 ± 33.1 nm, which is close
254 to this study's higher-end particle size of 200 nm hygroscopicity measurement. Therefore, ACSM bulk aerosol
255 composition is the most suitable choice for discussing the hygroscopicity of these particles.

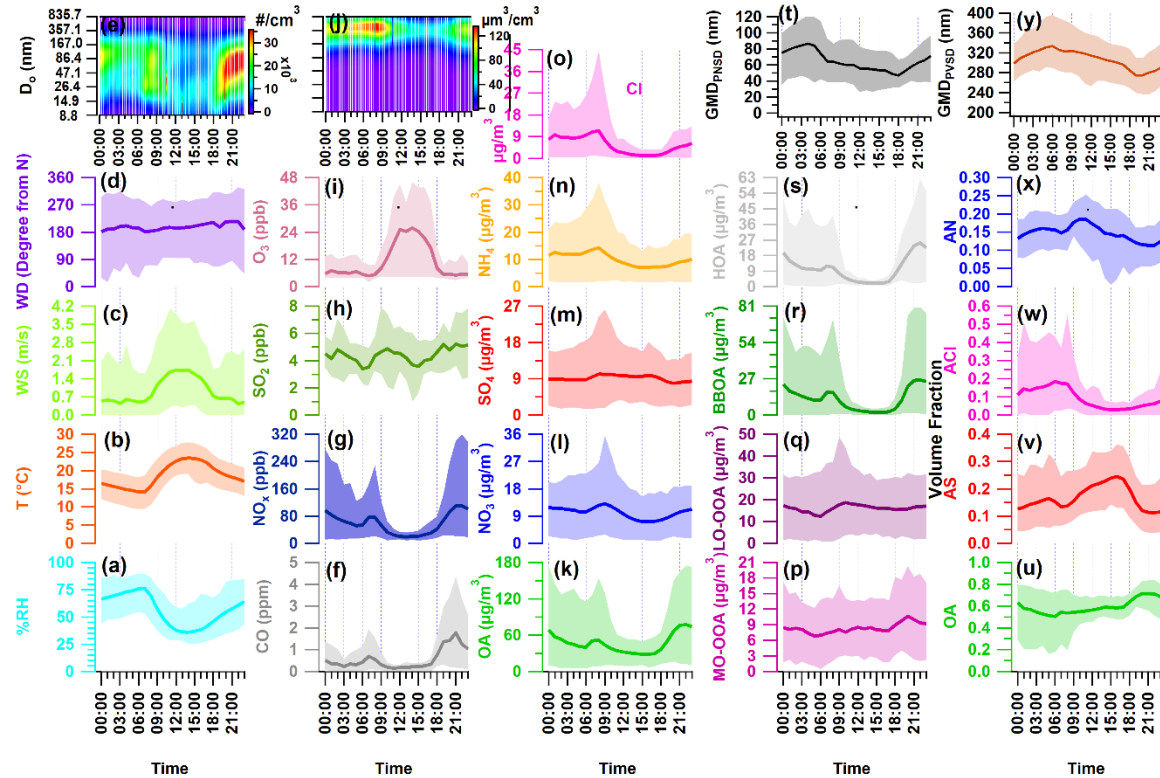
256 The hourly time-resolved NR-PM₁ (say hereafter PM₁) concentration varied from 9.0 to 357.9 $\mu\text{g}/\text{m}^3$, averaging
257 $81.2 \pm 56.6 \mu\text{g}/\text{m}^3$. This observation lies well within the boundary of 12.7-392 $\mu\text{g}/\text{m}^3$ (NR-PM₁), reported by Gani
258 et al. (2019) for the same sampling site. Prakash et al. (2018) reported that PM₁ mass concentration is 83% of
259 PM_{2.5}, representing the dominance of combustion-based particles. Further, we observed that ACSM measured
260 PM₁ was highly correlated ($r^2 = 0.83$, $p < 0.05$) with MPSS measured PM₁, assuming an effective aerosol density
261 1.6 g/cm³ (Fig. S2). The OA ranged between 1 and 293 (46.5 ± 39.6) $\mu\text{g}/\text{m}^3$ with the predominant fraction of PM₁,
262 consistent with the range of 53.3 to 166 (112) $\mu\text{g}/\text{m}^3$ observed during winter (December-February) at the same
263 site (Gani et al., 2019). However, lower average OA concentration could be explained by the measuring period of
264 February-March, as aerosol loading starts decreasing in February after reaching its peak in December-January
265 (Gupta and Mandariya, 2013). The campaign average fractional contribution OA to PM₁ was 56%, ranging from
266 1 to 84%. This high OA contribution in PM₁ is consistent with other studies conducted in IGP (Chakraborty et al.,
267 2016a; Gani et al., 2019; Mandariya et al., 2019) and worldwide (Jimenez et al., 2009; Zhang et al., 2007). Peaked
268 OA mass concentrations were noted between 21:00-23:00 hr (figure 2(k)), consistent with previous studies

269 conducted at the current site (Gani et al., 2019; Rai et al., 2020). Campaign average mass concentration of NO_3
270 was $10.1 \pm 7.0 \text{ }\mu\text{g/m}^3$ and showed diurnal variation with a peak in the morning and midnight (Fig. 3(l)). Besides,
271 SO_4 showed slight enhancement at 08:00 hr and remained nearly constant from noon to 17:00 hr (Fig. 3(m)).
272 However, Cl^- varied between 0.13 to $77.83 \text{ }\mu\text{g/m}^3$, and higher concentrations of Cl^- were found episodic throughout
273 the campaign. The Cl^- concentration was found consistent with Gani et al., 2019's previously reported value of
274 $0.1\text{--}66.6 \text{ }\mu\text{g/m}^3$ at the same site. The temporal variation of various OA factors is presented in Fig. 2(g and h).
275 Biomass burning organic aerosol (BBOA) mass concentration peaks during the night and morning hours (Fig.
276 3(r)). Low-volatility oxygenated organic aerosol (LO-OOA) exhibits a peak in the morning and remains relatively
277 constant at noontime, suggesting steady formation. Meanwhile, moderately oxygenated organic aerosol (MO-
278 OOA) shows a slight increase around noontime, indicating formation through daytime photooxidation (Mandariya
279 et al., 2019; Sun et al., 2016). Overall, oxygenated organic aerosol (OOA) was the dominant fraction of OA during
280 the sampling period. The H-BB events displayed a dynamic variation in BBOA mass concentration, ranging from
281 16.3 to 134.7 (averaging $50.7 \pm 24.0 \text{ }\mu\text{g/m}^3$). Concurrently, these events also exhibited a higher concentration of
282 HOA (ranging from 9.6 to $109.4 \text{ }\mu\text{g/m}^3$), suggesting a potential similarity in the sources of HOA during this
283 occurrence. However, during H-HOA events, a higher concentration of HOA (ranging from 4.8 to $58.9 \text{ }\mu\text{g/m}^3$)
284 was observed, although these concentrations were notably lower than those observed during H-BB events.
285 Nevertheless, fractional mass contribution of HOA to OA was largest among all OA species. Furthermore, H-Cl
286 events exhibited elevated concentrations of both primary organic aerosol HOA and BBOA. BBOA contributed
287 approximately 40.0%, 21.1%, 32.5%, and 13.1% to OA during H-BB, H-HOA, H-Cl, and relatively clean events,
288 respectively, suggesting diverse sources of BBOA. Moreover, during the H-HOA event, HOA's average
289 contribution was the highest among all events, at 41.6%. Additionally, Cl^- 's fractional mass contribution in PM_1
290 reached up to 44.9% during the H-Cl event, in contrast to 21.2% in H-BB events and 7.3% in H-HOA events.



291

292 **Figure 2: Temporal variability of ambient (a) relative humidity (RH), temperature (T), (b) wind speed (WS), wind**
 293 **direction (WD), (c) particle number-size distribution (PNSD), 24-average geometric mean diameter (GMD), (d) particle**
 294 **volume-size distribution (PVSD), (e) particulate matter (PM₁), organic aerosol (OA), nitrate (NO₃), sulfate (SO₄),**
 295 **ammonium (NH₄), chloride (Cl), (f) fractional contribution of OA, NO₃, SO₄, NH₄, and Cl in PM₁, (g) more oxidized-**
 296 **OA (MO-OOA), less oxidized-oxygenated OA (LO-OOA), biomass burning OA (BBOA), hydrocarbon like-**
 297 **OA (HOA), and (h) fractional contribution of MO-OOA, LO-OOA, BBOA, and HOA in OA. The pie chart sub-plot**
 298 **represents the overall average contribution of species, and the bar sub-plot represents the overall campaign average**
 299 **value of different species. All other species are represented with specific color coding mentioned in legends. The light**
 300 **green, pink, and grey color shaded vertical line indicates the high-BBOA (H-BB), high-HOA (H-HOA), and high-Cl**
 301 **(H-Cl) events, respectively. The discontinuity in the data points marks the missing data or non-sampling time.**



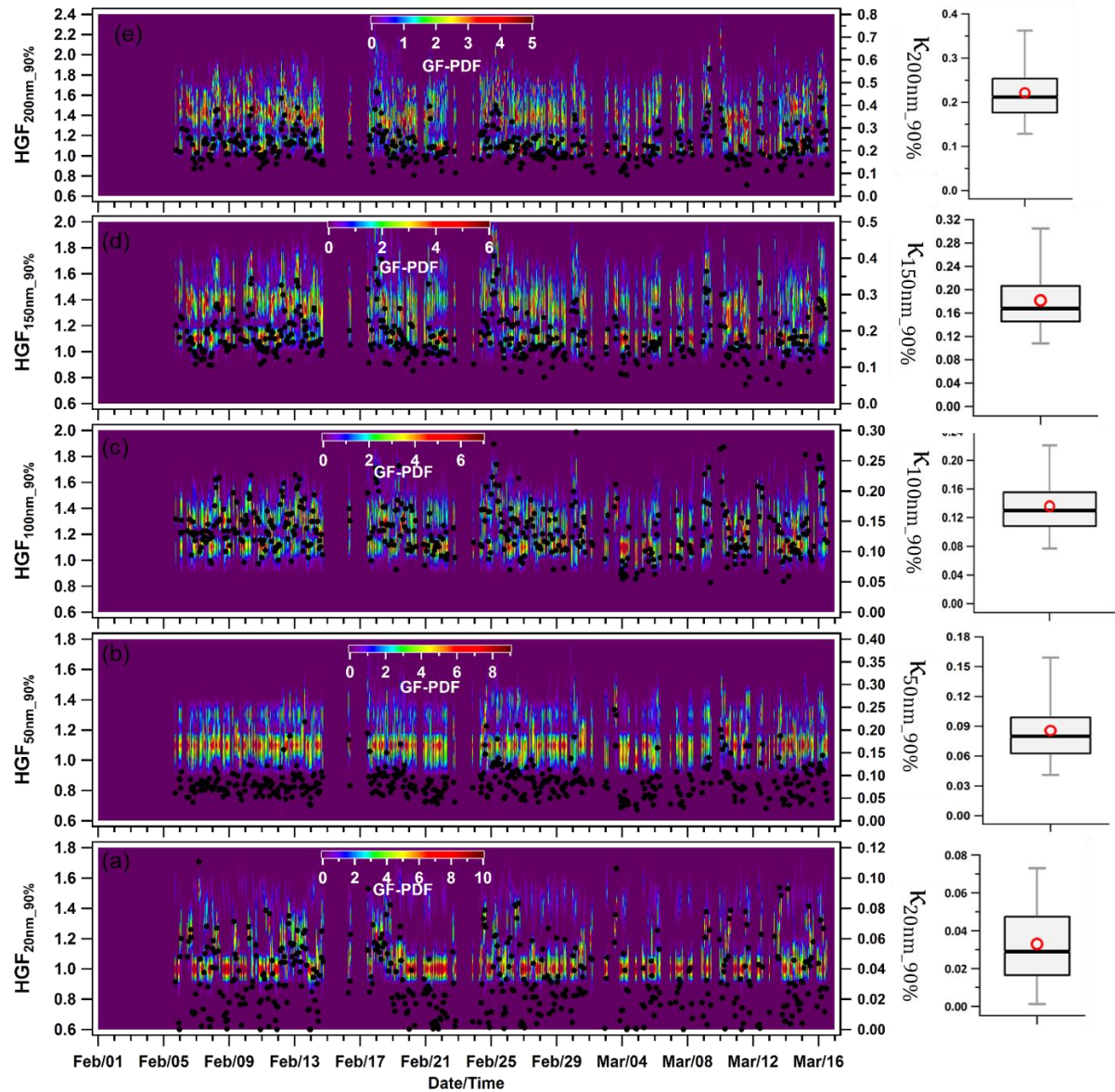
304 Figure 3: Diurnal variation of ambient meteorological parameters (a) % ambient relative humidity (RH), (b)
305 temperature (T), (c) wind speed (WS), (d) wind direction (WD), and (e) particle number size distribution (PNSD), mass
306 concentration of ambient trace gases (f) carbon mono-oxide (CO), (g) nitrogen oxides (NO_x), (h) sulfur dioxide (SO₂),
307 and (i) ozone (O₃), (j) particle volume size distribution (PVSD), mass concentration of aerosol constituents (k) organic
308 aerosol (OA), (l) nitrate (NO₃), (m) sulfate (SO₄), (n) ammonia (NH₄), and (o) chloride (Cl), mass concentration of
309 organic aerosol species (p) more oxidized-oxygenated OA (MO-OOA), (q) less oxidized-oxygenated OA (LO-OOA), (r)
310 biomass burning OA (BBOA), and (s) hydrocarbon like-OA (HOA), (t) geometric mean diameter of particle number
311 size distribution (GMD_{PNSD}) and volume fractional contribution of (u) organic aerosol (OA), (v) ammonium sulfate
312 (AS), (w) ammonium chloride (ACI), and (x) ammonium nitrate (AN) in PM₁, and (y) geometric mean diameter of
313 particle volume size distribution (GMD_{PVSD}). Upper and lower boundary of shaded area represents the 95th and 5th
314 percentile values of respective species.

315 3.2 Hygroscopicity of Nucleation, Aitken, and Accumulation Mode Particles

316 3.2.1 Temporal variability

317 Fig. 4 shows the dynamic variability in the hourly averaged HGF_{90%} and hygroscopicity parameter ($\kappa_{H-TDMA-90\%}$,
318 kappa) of Nucleation, Aitken, and Accumulation mode aerosol particles at 90% ambient relative humidity. The

319 hygroscopic growth factors of 20 (HGF_{90%_20nm}), 50 (HGF_{90%_50nm}), 100 (HGF_{90%_100nm}), 150 (HGF_{90%_150nm}), and
320 200 nm (HGF_{90%_200nm}) size particles varied between 1.00-1.41, 1.05-1.39, 1.11-1.49, 1.12-1.63, and 1.12-1.79
321 with an average of 1.14 ± 0.09 (average \pm standard deviation), 1.16 ± 0.06 , 1.27 ± 0.07 , 1.35 ± 0.09 , and $1.41 \pm$
322 0.09, respectively. These mean hygroscopic growth factors were noted as statistically ($p < 0.05$) different from each
323 other. In addition, the hygroscopicity ($\kappa_{20nm_90\%}$ and $\kappa_{50nm_90\%}$) of 20 and 50 nm aerosol particles varied between
324 0.00-0.11 and 0.02-0.25, with an average of 0.03 ± 0.02 and 0.09 ± 0.03 , respectively. Nucleation mode particles
325 were observed, mainly monomodal GF-PDF (Fig. 4(a)), comprising nearly 74 \pm 24% nearly hydrophobic particles
326 (HGF < 1.2). However, this contribution was raised to 100%, which was observed to have a good association with
327 night-time local burning activities, as shown in the Fig. 4(a). The nucleation mode particles ($\kappa_{20nm_90\%}$) showed
328 significantly ($p < 0.05$) lower hygroscopicity than Aitken mode particles ($\kappa_{50nm_90\%}$). Hong et al. (2015) reported
329 that nucleation mode particles are more sensitive to condensable vapors like fresh VOCs, H₂SO₄ and HCl.
330 However, the present study did not measure these species. The κ of Aitken size particles were comparable with
331 0.24 ± 0.08 of 52.6 ± 6.9 size particles reported by Gunthe et al. (2011) for Beijing. Beijing is also one of the most
332 polluted urban locations like Delhi, which could justify the comparison. However, Gunthe et al. (2011) performed
333 this study using CCN on supersaturation levels. The campaign average hygroscopicity parameter (kappa, $\kappa_{90\%}$)
334 increased significantly ($p < 0.05$) with particle size, which can be attributed to the kelvin effect (Wang et al., 2018a).
335 In the accumulation size range (100, 150, and 200 nm), $\kappa_{90\%}$ increased to ~ 0.56 . The overall sampling average
336 values of $\kappa_{100nm_90\%}$, $\kappa_{150nm_90\%}$, and $\kappa_{200nm_90\%}$ were 0.14 ± 0.04 , 0.18 ± 0.06 , and 0.22 ± 0.07 , respectively. The
337 $\kappa_{200nm_90\%}$ varied between 0.05 and 0.56. The similar kind of variation in κ with particle size has been demonstrated
338 in Kanpur, situated at the center of IGP, India (Mandariya et al., 2020a) and worldwide studies (Cerully et al.,
339 2015; Enroth et al., 2018; Fan et al., 2020; Kawana et al., 2016; Kim et al., 2020; Kitamori et al., 2009; Ogawa et
340 al., 2016; Sjogren et al., 2012; Wang et al., 2018a). Moreover, this was attributed to the predominant increment
341 in inorganic to OA fraction in particles with increment in size. Furthermore, $\kappa_{H-TDMA_90\%}$ was found approximately
342 in the 0.13-0.77, reported by Arub et al. (2020) at Delhi for PM₁ without considering BC. Although, Arub et al.
343 (2020) theoretically predicted particles' hygroscopicity by considering a particle's chemical composition. They
344 found a decrease in κ calculation by 10% when BC was considered in aerosol chemical composition. Also, $\kappa_{H-TDMA_90\%}$
345 measured in the current study were found in line with the global average value of 0.27 ± 0.21 for
346 continental aerosols (Petters and Kreidenweis, 2007; Pringle et al., 2010). Further, to understand the impact of a
347 particle's chemical composition, local meteorology, and air mass trajectories on $\kappa_{H-TDMA_90\%}$ for accumulation
348 mode particle discussed in subsequent sections.



351 **Figure 4: Temporal variability in hygroscopic parameter kappa (κ) of nucleation mode particles (a) 20 nm ($\kappa_{20\text{nm_90\%}}$),**

352 Aitken mode particles (b) 50 nm ($\kappa_{50\text{nm_90\%}}$), and Accumulation mode particles (c) 100 nm ($\kappa_{100\text{nm_90\%}}$), (d) 150 nm

353 ($\kappa_{150\text{nm_90\%}}$), and (e) 200 nm ($\kappa_{200\text{nm_90\%}}$). The box plots represent the variability in the hygroscopicity of respective sizes

354 of particles in which low and high whisker traces represent the 5 and 95 percentile, respectively. The red marker

355 indicates the average of the data, whereas the upper and lower sides of the boxes indicate the 75 and 25 percentile of

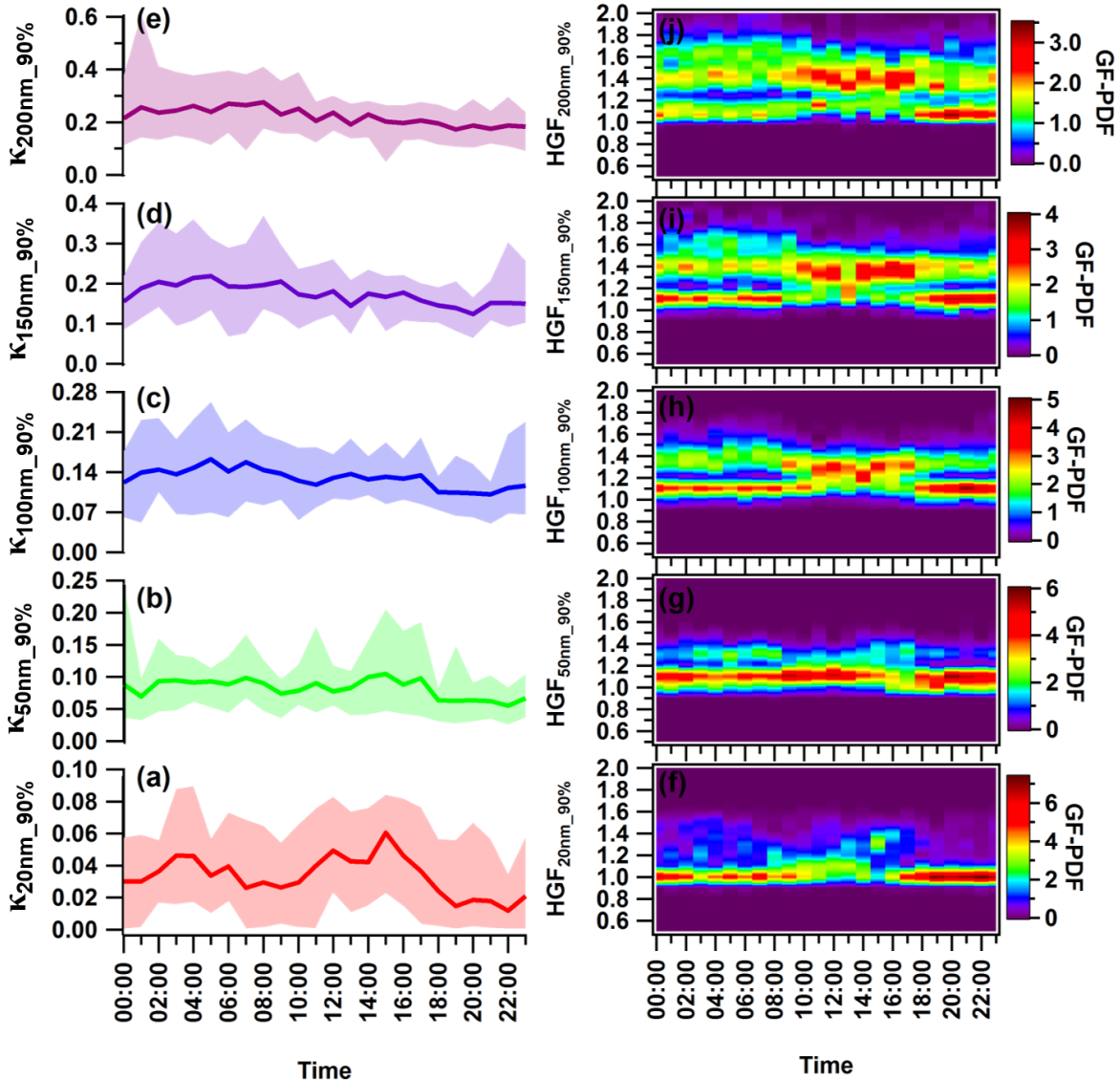
356 the data, respectively.

357 **3.2.2 Diurnal variability**

358 The diurnal variability in $\kappa_{\text{H-TDMA-90\%}}$ was found different for nucleation ($\kappa_{20\text{nm-90\%}}$), Aitken ($\kappa_{50\text{nm-90\%}}$), and
359 Accumulation ($\kappa_{100\text{nm-90\%}}$, $\kappa_{150\text{nm-90\%}}$, and $\kappa_{200\text{nm-90\%}}$) mode particles. Fig. 5 displayed a diel variation of an average
360 of hourly-resolved κ for each size. The bigger size particles exhibited higher values of κ than smaller size particles,
361 which is a similar trend reported at Kanpur, India (Mandariya et al., 2020a) and other worldwide locations (Fan
362 et al., 2020; Hong et al., 2015). In general, it was observed that all size particles exhibited late-night hump (02:00-
363 05:00 hr) in $\kappa_{\text{H-TDMA-90\%}}$. Besides, only $\kappa_{20\text{nm-90\%}}$ demonstrated a clear diurnal variability with two peaks, one late
364 night (02:00-04:00 hr) and the other in noontime (14:00-16:00 hr), and two valleys during the morning (07:00-
365 10:00 hr) and night (19:00-22:00 hr). These valleys reflects the strong impacts of local burning and traffic
366 activities (Pringle et al., 2010). In addition, nucleation size particles were potentially contributed by nearly
367 hydrophobic particles (HGF<1.2) from evening to midnight. They showed mono modal GF-PDF around unit
368 hygroscopic growth factor, possibly indicating local emission generated particles. The 20 nm particles are small
369 enough and lie on the boundary of nucleation mode particles. Achtert et al. (2009) reported a similar diurnal trend
370 of Nucleation and Aitken mode particles, attributed the lower values to the emission of hydrophobic aerosol
371 particles during the local burning emissions. Daytime hump is attributed to the intense photochemical oxidation
372 process, which causes the enhancement of more oxidized species on the aerosol particle. Furthermore, their
373 chemical composition is dominantly controlled by the gaseous condensation of H_2SO_4 , HNO_3 , and VOCs (Hong
374 et al., 2015). The aerosol's chemical composition can address this variability of $\kappa_{\text{H-TDMA-90\%}}$. However, $\kappa_{50\text{nm-90\%}}$
375 also follows a similar diurnal variability as $\kappa_{20\text{nm-90\%}}$, although it showed less variability. Further, as the dry size
376 of the aerosol particles increased to accumulated mode, diurnal variation shifted toward nearly steady for the rest
377 of the day. Hong et al. (2018) also observed no obvious diurnal pattern for 100 and 150 nm particles of organic-
378 dominated aerosols over the Pearl River Delta region in China.

379 Furthermore, the diurnal cycles of aerosol physicochemical properties also reflect the dynamic diurnal variation
380 in the planetary boundary layer (PBL) that leads to the accumulation of particles during night-time. Although this
381 study did not quantify size-resolved chemical composition, so, this study used bulk-aerosol composition to address
382 the trend variability only. However, daily average aerosol PNSD varied between 18.0-140.0 nm with a mean of
383 73.1 ± 33.8 nm. And, the mode of PVSD changed approximately around 300-600 nm. Therefore, it could be an
384 excellent approximation to discuss $\kappa_{200\text{nm-90\%}}$ variability with aerosol's bulk chemical properties. The midnight to
385 early morning hump in hygroscopicity of accumulation mode particles can be attributed to the high rise in the
386 ratio of inorganic volume fraction to OA volume fraction (Fan et al., 2020), as illustrated in figure 2 (r, s t, u, and
387 v). Moreover, during mid-night and early morning in the winter, water-soluble organic and inorganic gases are

partitioned and/or coagulated/condensed on the surface of the pre-existing particles. Further, in the presence of high RH and lower temperature, primary and secondary less oxidized organic aerosol participated in the aging process, which leads to enhancement their oxidation via aqueous/heterogeneous reaction, according to it increase the particle's hygroscopicity (Jimenez et al., 2009; Wu et al., 2016). Similar results were observed by Fan et al. (2020) during winter in urban Beijing, and they attributed it with the enhancement of more hygroscopic particles due to the aqueous-oxidation and/or condensation process on the pre-existing particles. In general, higher noontime solar radiation favours more intense photooxidation processes. It supports the partitioning of relatively more oxidized and less volatile organics on the particulate surface, enhancing the hygroscopicity of accumulation mode particles (Duplissy et al., 2011; Massoli et al., 2010; Tritscher et al., 2011). However, interestingly, we observed a noontime flatten pattern of $\kappa_{\text{H-TDMA_90\%}}$, and it could be attributed to the mix of the positive and negative impact of an enhancement in the volume fraction of OA and more hygroscopic ammonium sulfate and decrement in ACl, and AN's volume fraction. Lower volume fractional contribution of highly volatile ACl could be the potential factor that modulates accumulation mode particle's hygroscopicity. This can be supported by the strong correlation of $\kappa_{\text{H-TDMA_90\%}}$ and volume fraction of ACl in that size particles (ε_{ACl}).



402

403 **Figure 5: Diurnal variance in the hygroscopic parameter kappa (κ) of nucleation mode particles (a) 20 nm ($\kappa_{20\text{nm_90\%}}$),**

404 Aitken mode particles (b) 50 nm ($\kappa_{50\text{nm_90\%}}$), and Accumulation mode particles (c) 100 nm ($\kappa_{100\text{nm_90\%}}$), (d) 150 nm

405 ($\kappa_{150\text{nm_90\%}}$), and (e) 200 nm ($\kappa_{200\text{nm_90\%}}$) and hygroscopic growth factor of (f) 20 nm ($\text{HGF}_{20\text{nm_90\%}}$), (g) 50 nm

406 ($\text{HGF}_{50\text{nm_90\%}}$), (h) 100 nm ($\text{HGF}_{100\text{nm_90\%}}$), (i) 150 nm ($\text{HGF}_{150\text{nm_90\%}}$), and 200 nm ($\kappa_{200\text{nm_90\%}}$) aerosol particles. The

407 solid line represents diurnal average values, and the upper and lower shaded area represents 95 and 5 percentile values

408 of corresponding average values. Different color coding has been used to represent various size-specific kappa values.

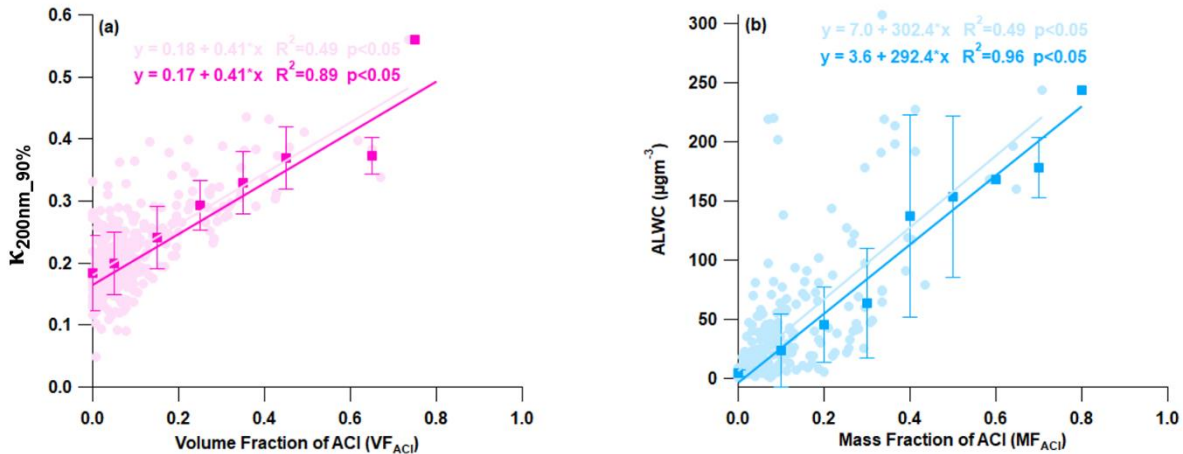
409 The color scale represents the growth factor probability density function of hygroscopic growth factor.

410 3.2.3 Driving Factor of Hygroscopicity

411 A correlation analysis was carried out between measured chemical species and aerosol to explore the factors

412 governing aerosol hygroscopicity, as shown in the Fig. 6. Organic aerosol was observed negatively impact κ ,

413 explained by a negative correlation (Fig. S7(a)). This negative correlation of OA with κ is also observed in India
414 (Bhattu et al., 2016; Mandariya et al., 2020b) and worldwide (Enroth et al., 2018; Hong et al., 2014; Kawana et
415 al., 2016; Kitamori et al., 2009; Wang et al., 2018a; Wu et al., 2013a). This result indicates that primary
416 constituents dominated the OA during high loading, considered nearly hydrophobic or less hygroscopic. In
417 addition, the current study observed that an enhancement of 10% of OA by volume in 200 nm aerosol particles
418 would be responsible for a 4% decrement in its hygroscopicity (Fig. S7(a)). Interestingly, ammonium sulfate and
419 nitrate showed a positive but poor correlation with hygroscopicity (Fig. 7(b and c)). It could be due to sulfate and
420 nitrate aerosol dominating the bigger particles (>200nm). However, a 10% enhancement of AS by volume was
421 found to be responsible for the enhancement of hygroscopicity only by 1.6%. But if AS contribution increased in
422 the aerosol composition, aerosol water-bound capacity was negatively impacted (Fig. S8b) Besides, Fig. 6(a)
423 shown an increasing volume fraction of ACI in PM_1 with an increase in aerosol hygroscopicity, and this strong
424 positive correlation is responsible for an enhancement in κ by 4.2% over the increment of 10% ACI by
425 volume, which was the highest among all chemical species. Further, ammonium chloride has a more significant
426 water uptake potential (Chen et al., 2022; Zhao et al., 2020), which can be justified by the solid correlation of
427 aerosol liquid water content (ALWC) with a mass fraction of ACI in PM_1 as shown in Fig. 6(b). This indicates
428 that particles with a more considerable ammonium chloride fraction uptake more water vapor, leading to higher
429 hygroscopic aerosol particles. It is clear that the increases in ammonium chloride fraction enhanced aerosol liquid
430 water content and led to higher hygroscopicity of aerosol particles. A Recent study in Delhi by Chen et al. (2022)
431 unveils that ammonium chloride fraction in PM_1 aerosol enormously enhances during the higher relative humidity
432 conditions during the winter season due to the co-condensation of semivolatile ammonium chloride with water
433 vapor on the particles and leads to enhance water uptake and lead severe winter haze in Delhi. The very high
434 volume fractions (>30%) of ACI in atmospheric PM_1 were observed episodic, suggesting a high fraction of Cl in
435 the particle phase is strongly dependent on excess ammonia in the atmosphere. These results indicate that ammonia
436 is the controlling factor for chloride partitioning in the particle phase, resulting in high aerosol water content under
437 high RH and lower temperature conditions. As the ACI is strongly dependent on the RH and temperature.



438

439 **Figure 6: Correlation plot for (a) $\kappa_{200\text{nm}}\text{--}_90\%$ vs volume fraction of ammonium chloride aerosol (VF_{ACI}) and (b) aerosol**

440 liquid water content (ALWC) vs mass fraction of ammonium chloride (MF_{ACI}). The solid circle and square marker

441 represent the individual data points and the average of 10% volume and mass fraction increment of ACI data points,

442 respectively. The light and dark color regression lines and equations indicate the overall and average (10% volume and

443 mass fraction increment) correlation, respectively. The error bars indicate the standard deviation of the data points

444 within the 10% mass and volume fractional bins.

445 **3.2.4 Hygroscopicity during high biomass burning (H-BB), high-hydrocarbon like OA (H-HOA), high-Cl**

446 **(H-Cl), and relatively Clean Periods**

447 Delhi's atmosphere is a complex array of chloride and organic aerosol sources like combustion (crop residue,

448 agriculture waste, medical waste, municipal waste, plastic, etc., burning) and industrial sources. Therefore, all

449 episodic events were classified into three to investigate the impact of chloride and OA on aerosol hygroscopicity.

450 First, high biomass burning (H-BB) event; second, high-hydrocarbon like OA (H-HOA) event; and third, high-Cl

451 (H-Cl) events. Further, aerosol chemical composition data were filtered according to hygroscopic parameter data

452 for further analysis. By performing so, data information that is characteristic of the local emission and atmospheric

453 chemistry in question and the effects of various potential transported air mass types can be retrieved. It is valuable

454 to extract any possible information about aerosol sources and transformation process evaluation to interpret its

455 influence on the aerosol's hygroscopicity.

456 **3.2.4.1 High-Cl (H-Cl) events**

457 H-Cl events, representing the substantial loading of ACI on the receptor site, were chosen mainly due to the

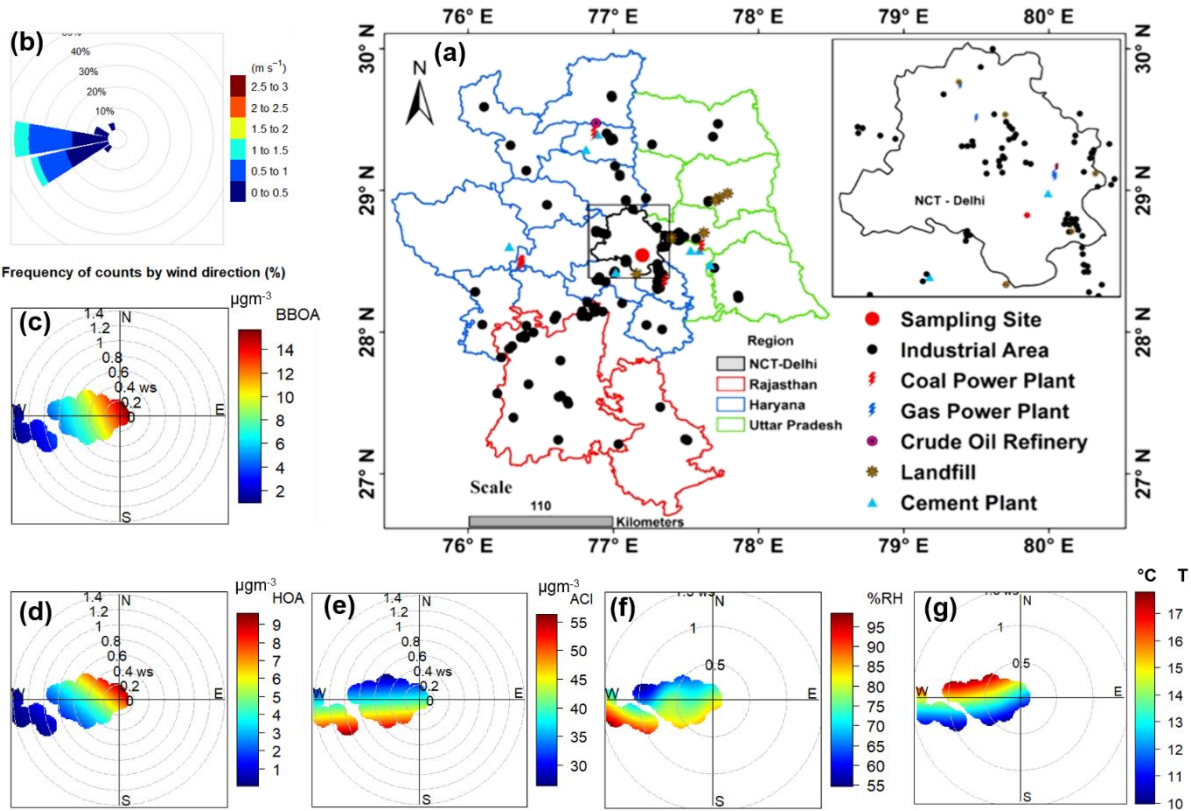
458 significant jump (>20%) in fractional volume contribution NH_4Cl (ε_{ACI}) in the PM_1 aerosol. This period observed

459 apparent surface wind from W-direction, although WNW, WSW, and SE winds also influence the site, as shown

460 in Fig. 7b. The average GMD of the PNSD was nearly 64 nm, indicating that local fresh emissions sources
461 influence the particles. In addition, the mean SO_2 , NO_x , and CO concentrations were at 3.6 ppb, 51.9 ppb, and 0.4
462 ppm, respectively. BBOA and HOA are potentially contributed from the WNW and SE directions, as explained
463 in the bipolar plot Fig. 7(c & d), and seem to come from a similar local source. Among inorganic species, ACl
464 observed excellent association with ambient RH, as shown in Fig. 7e and f, indicating the atmospheric gaseous
465 HCl neutralized with NH_3 gas in the presence of atmospheric water content. HCl sources could be coal power
466 plants, trash burnings in solid waste dumping sites, and other industries located in the W-WSW direction (Gani et
467 al., 2019), as shown in the map in Fig. 7a. Atmospheric high Cl events are potentially dominated by trash burning
468 in Delhi during winter (Shukla et al., 2021; Tobler et al., 2020). Moreover, bipolar plots (figure 6(e and f)) suggest
469 that ACl formation under high RH conditions associated with a relatively calm atmosphere trigger particles'
470 hygroscopicity. This hypothesis can be supported with a good association of aerosol liquid water content (ALWC)
471 as discussed in previous section. Furthermore, GF-PDF of all size particle marked relatively more fractionaly
472 contribution of secondary mode particles as showed in Fig. 8d. Overall more hygroscopic ($\text{HGF90\%}>1.2$)
473 particles were marked by 42, 47, 50, 74, and 83% contributions in the 20, 50, 100, 150, and 200 nm size particles,
474 respectively. Hence, ACl is a critical factor to enhance aerosol hygroscopicity to trigger fog/haze formation under
475 higher RH and colder atmospheric conditions as discussed in the previous section.

476 Similarly, Gunthe et al. (2021) observed that high local emission of hydrochloric acid in Delhi during February-
477 March gets partitions into aerosol liquid water under high humid conditions, enhancing the water uptake capacity
478 of aerosol sustain particle's hygroscopic growth, result in fog/haze formation. Moreover, worldwide studies on
479 size-resolved hygroscopicity observed Cl less than 1%, so they omitted ACl as an aerosol constituent into the
480 discussion. In addition, the current study did not find any strong correlation of κ with AS and AN. It could be due
481 to their association with larger particle sizes. Besides, ACl could be associated with comparatively lower size
482 particles (≤ 200 nm). Furthermore, in context to look influence of air mass trajectories, we further mapped
483 aerosol's constituents in the association of air mass back trajectories in PSCF to see the potential area source
484 contribution influencing the aerosol evaluation processes, ultimately aerosol's hygroscopicity. However, we did
485 not find any back trajectory influencing the receptor site, as all trajectory endpoints were observed above the
486 planetary boundary layer height.

487



488

489 **Figure 7** Map of (a) Delhi showing various types of industries located in the region and nearby locations, (b) wind rose
 490 diagram and conditional bi-polar plots showing variation in mass concentration of (c) biomass burning OA (BBOA),
 491 (d) hydrocarbon like OA (HOA), (e) ammonium chloride (ACI), (f) % ambient relative humidity (RH), and (g) ambient
 492 temperature (T), with wind direction (WD) and wind speed (WS) during H-Cl events. A background map showing
 493 various industrial locations was adapted from Rai et al. (2020).

494 **3.2.4.2 High biomass burning (H-BB) Events**

495 High BB events were noted during the initial period (1-12 February) of the field campaign. However, H-BB events
 496 were generally captured either during the midnight (01:00 hours) to morning (08:00 hours) or evening (20:00
 497 hours) to midnight (01:00 hours). Although, sometimes, it was continued from evening (21:00 hours) to morning
 498 (11:00 hours). The predominant surface wind circulations were from W, W-WNW, and W-WSW directions (Fig.
 499 S9b). The aerosol was dominated by local emissions, as aerosol constituents are mainly associated with slower
 500 wind circulations from landfill sites, industrial areas, and coal power plants, as shown in Fig. S9a. Further, it could
 501 justify the potential source contribution function (PSCF) analysis considering 48-hr air mass back trajectories, as
 502 shown in Fig. S10. The average GMD of the PNSD was nearly 87 nm. In addition, the mean SO₂, NO_x, and CO
 503 concentrations were at 4.7 ppb, 124.1 ppb, and 1.5 ppm, respectively. Therefore, BBOA possibly contributed from
 504 the open local biomass burning activities at landfill sites or others. Organic aerosol in the H-BB event confined

505 the most considerable fraction, 39%, of BBOA, following HOA, 28%. Figure S9 (b, c, and d) clearly shows that
506 BBOA and HOA have similar local source profiles but differ from the ACI source. Moreover, ACI was not found
507 to have a good association with ambient RH and but was associated with nearby coal power plant's emissions.
508 However, 48 h air mass back trajectories indicated that the current city was also influenced by air mass from some
509 parts of Uttar Pradesh, Punjab, and Haryana. These states are the potential hub of crop residue burning, industrial
510 activities and brick kilns. These cities have a substantial fraction of OA in PM_1 and OA mainly affected by biomass
511 activities during winter. The H-BB event captured a considerable volume fraction, 71% of OA in PM_1 and BBOA
512 contributed almost 39%, as illustrated in the Fig. 9. So, lower inorganic to OA ratio was a potential factor in
513 decreasing the aerosol hygroscopicity in H-BB events. Further, a primary organic aerosol contribution was
514 enhanced during this event and, on average, raised to 67%. OA loading inversely affects the aerosol's
515 hygroscopicity. Mandariya et al. (2020) reported a similar observation in Kanpur, and the authors suggested that
516 the contribution of primary biomass burning (BBOA) and hydrocarbon-like OA adversely affects aerosol
517 hygroscopicity. BBOA showed a good negative correlation with the hygroscopicity of 200 nm particles,
518 supporting the following conclusion. Apart from this, the Nucleation size particle (20 nm) showed 0.02 ± 0.02
519 hygroscopicity parameter with mono mode GF-PDF with the unit mode (Fig. 8b) and confined $83.7 \pm 18.6\%$
520 nearly hydrophobic particles. Furthermore, as aerosol size increased, hygroscopicity parameter ($\kappa_{H-TDMA_90\%}$)
521 enhanced significantly ($p < 0.05$) as the contribution of relatively secondary aerosol particles ($GF > 1.2$) increased
522 with aerosol size. Accumulation size aerosol, 100 nm contributed approximately 54% by nearly hydrophobic
523 ($GF < 1.2$) and 46% by more hygroscopic ($GF > 1.2$) particles.

524 **3.2.4.3 High-HOA (H-HOA) Events**

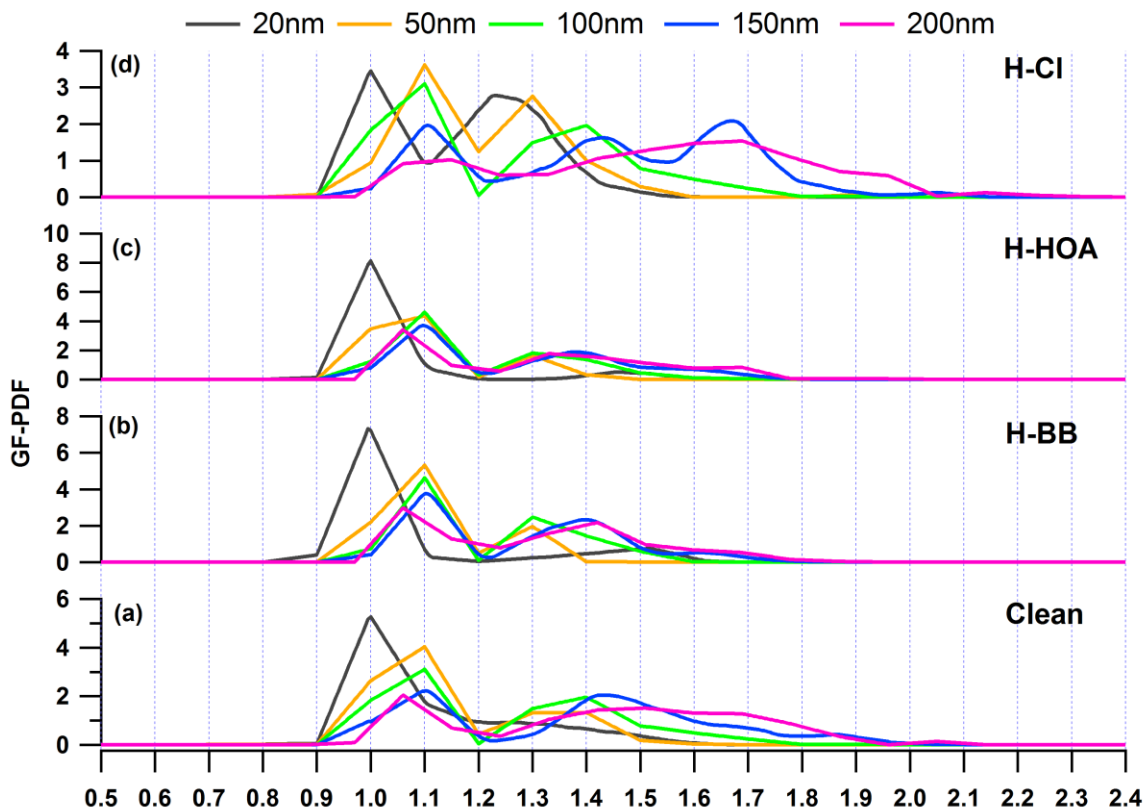
525 H-HOA events were identified based on the considerable mass concentration and fraction of HOA in the organic
526 aerosol. These periods were noted generally 19:00 hr to Morning 09:00 hr during 22-23 and 26-27 February and
527 4, and 7-8 March as indicated in Fig. 2. The average GMD of the PNSD was nearly 80 nm. In addition, the mean
528 SO_2 , NO_x , and CO concentrations were at 4.3 ppb, 136.7 ppb, and 1.1 ppm, respectively. PSCF explore the
529 probability of impacts of long-range transported aerosol. Interestingly, it was observed that air masses over Delhi,
530 Haryana, and Uttar Pradesh were potentially associated with hydrocarbon-like OA (Fig. S11). BBOA also
531 followed a similar path as HOA. However, the potential area source of ACI was the nearby region of Delhi and
532 Haryana. The HOA loading was significantly ($p < 0.05$) higher than in H-BB, H-Cl and Clean periods. However,
533 emission sources were different during both H-HOA and H-BB periods. As HOA was the potential contributor to
534 OA, it is likely the critical constituent to modulate aerosol hygroscopicity in the region during these events. HOA

535 is mainly considered hydrophobic (Duplissy et al., 2011). Therefore, elevated HOA contribution (41%) in OA
536 could be responsible for lower κ in these events. The overall hygroscopicity of 20, 50, 100, 150, and 200 nm size
537 particles was recorded as 0.01 ± 0.01 , 0.06 ± 0.03 , 0.11 ± 0.03 , 0.14 ± 0.04 , and 0.17 ± 0.05 , respectively. The
538 predominant fractional contribution of primary aerosol particles (GF<1.2) seems to be a reason for this lower
539 hygroscopicity of particles, as shown in figure 7(c). Overall, OA predominantly constitutes the fraction in the
540 PM_1 , and primary OA contributed approximately 60% in OA. However, relative increment in the contribution of
541 other more hygroscopic constituents like secondary organic aerosol (LO-OOA and MO-OOA), ACl and
542 ammonium sulfate (AS) in the aerosol possible tried to balance the negative impact high-HOA on which limited
543 κ .

544 **3.2.4.5 Relatively Clean Period**

545 The 24th and 25th of February and the 5th, 6th, and 7th of March were marked as clean events. The night 21 hour to
546 morning 11-hour duration was recorded as the clean duration. The relatively clean period was predominantly
547 dominated by E, S-E winds; however, pollution was associated with calm winds, as illustrated in Fig. S9. The
548 average GMD of the PNSD was nearly 54 nm. In addition, the mean SO_2 , NO_x , and CO concentrations were at
549 4.2 ppb, 43.2 ppb, and 0.4 ppm, respectively. All BBOA, HOA, and ACl were observed to be associated with
550 similar sources and found an excellent association with ambient relative humidity. The mean concentration of
551 organic aerosol, ACl, AN, and AS was observed at 11.0 ± 6.4 , 1.4 ± 1.1 , 3.0 ± 1.5 , and $4.4 \pm 2.2 \mu\text{gm}^{-3}$,
552 respectively. These mass concentrations were significantly lower than in other specified periods. However, OA
553 was still the dominant species, with 56% by volume in the PM_1 , as indicated in Fig. 9. Among all OA factors,
554 HOA was predominantly dominated in OA with 33%, although secondary organic aerosol confined the overall
555 54.4% of OA. Secondary OA is defined with relatively higher oxidized OA, and the oxidation state of OA
556 positively impacts OA hygroscopicity (Kim et al., 2017; Richard et al., 2011; Wu et al., 2013a). The Clean period's
557 mean hygroscopicity of 20, 50, 100, 150, and 200 nm particles were observed at 0.03 ± 0.02 , 0.09 ± 0.04 , $0.14 \pm$
558 0.06 , 0.22 ± 0.09 , and 0.27 ± 0.07 , respectively, significantly ($p<0.05$) different to each other. However, the
559 accumulation particle's (200 nm) hygroscopicity was not significantly ($p>0.05$) higher than the 150 nm particles.
560 The hygroscopicity increment with size from 20 to 200 nm can also be explained by the fractional increment of
561 more hygroscopic (GF>1.2) particles relative to nearly hydrophobic or less hygroscopic particles (GF<1.2).
562 Nucleation particles, 20 nm was dominated mostly by less hygroscopic particles ($76.8 \pm 21.7\%$), indicates
563 influence by fresh emission sources, whereas, Aitken (50 nm) and Accumulation (200 nm) size aerosol were

564 confined with 69.3 ± 14.7 and 25.4 ± 10.8 less hygroscopic particles, respectively. These results point out that
 565 accumulation-size aerosols dominated secondary aerosols, which can also support their GF-PDF as shown in Fig.
 566 8(a). Nucleation size aerosol particles (20nm) showed nearly mono modal GF-PDF with the mode of unit growth
 567 factor. In contrast, the mode shifted towards the higher end as aerosol size increased and GF-PDF shifted from
 568 unit to multi-mode.



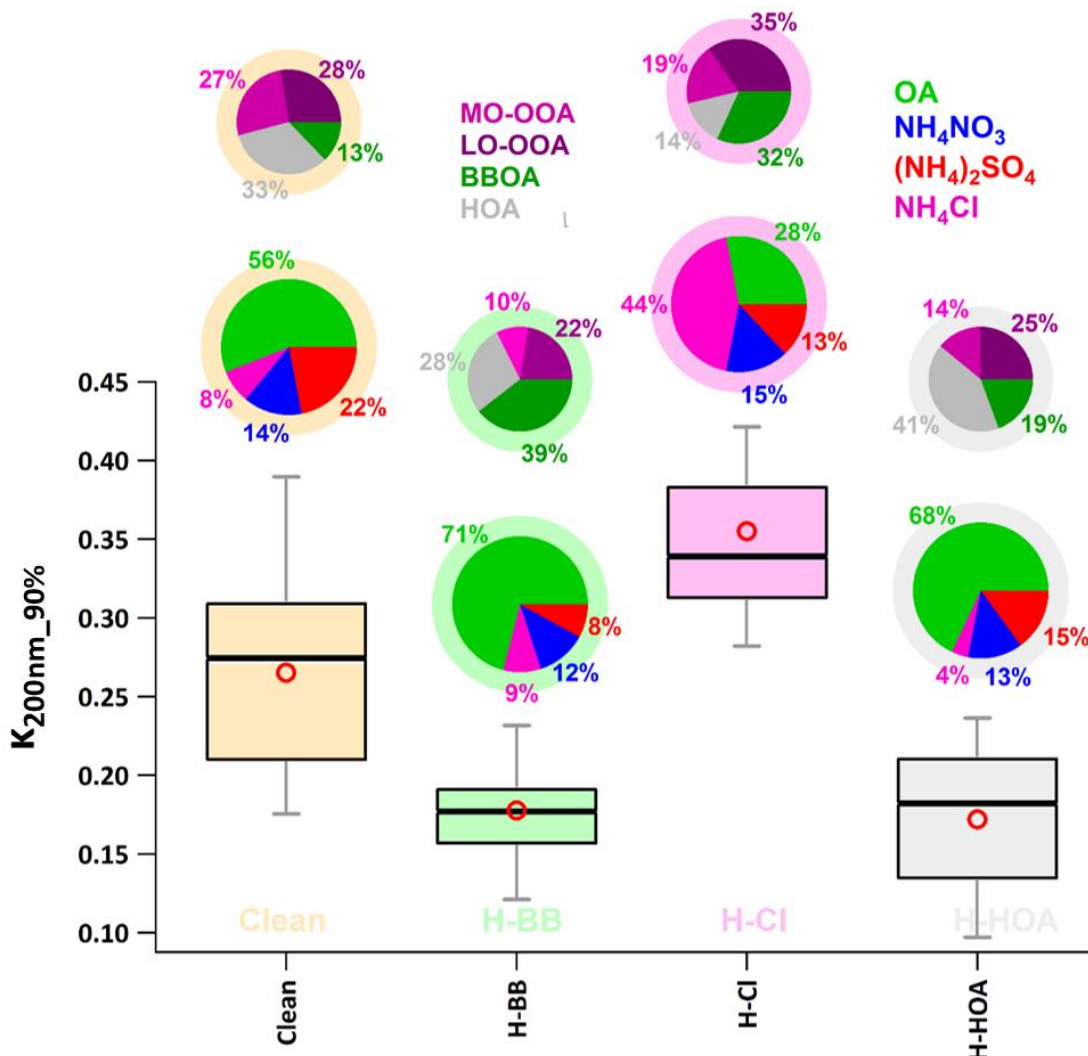
569
 570 **Figure 8: Growth Factor Probability Density Function (GF-PDF) of 20, 50, 100, 150, and 200 nm aerosol particles for**
 571 **the (a) clean, (b) H-BB, (c) H-HOA, and H-Cl periods.**

572 **3.2.4.6 Comparison of κ for different events**

573 We considered a 200 nm accumulation particle size particle representing the bulk aerosol chemical composition
 574 to compare the aerosol hygroscopicity among various periods. Further, in the present study, the mode of particle-
 575 volume size distribution varied from 400 nm to 600 nm particle dry mobility diameter. Therefore, 200 nm size
 576 accumulation particles are the best choice to compare hygroscopicity parameters among different periods
 577 considering bulk aerosol composition in various mentioned periods. In addition, a good Pearson's r value, 0.76,

578 was found among $\kappa_{200\text{nm_90\%}}$ and $\kappa_{\text{chem_90\%}}$, derived from the dry PM_1 particle's chemical composition measured
579 from the ACSM based on the ZSR mixing rule (Stokes and Robinson, 1966), which justifies our choice.

580 The H-Cl event noted the highest value (0.36 ± 0.06) of $\kappa_{200\text{nm_90\%}}$ against H-BB (0.18 ± 0.04), H-HOA ($0.17 \pm$
581 0.05), and Clean (0.27 ± 0.07) events, as illustrated in Fig. 9. The H-Cl event observed that the average $\kappa_{200\text{nm_90\%}}$
582 value was significantly ($p < 0.05$) higher than those observed in other events. It means that a substantial increment
583 in Cl emission in the Delhi region could significantly enhance the aerosol liquid water content leading to higher
584 aerosol hygroscopicity, which can further strengthen cloud condensation nuclei formation, possibly triggering
585 haze/fog events in Delhi NCR (Gunthe et al., 2021). These results suggest that controlling the open trash/waste
586 burning in the region could help control Cl emission, which leads to minimizing the haze/fog formation possibility
587 during high atmospheric conditions. However, the difference in $\kappa_{200\text{nm_90\%}}$ values between H-BB and H-HOA
588 events was not observed significantly ($p > 0.05$), possibly due to the relative changes in primary, secondary OA,
589 and inorganic species. In the H-HOA events, the negative effect of a significantly higher fractional (41%)
590 contribution of HOA to OA possibly balances with a positive impact of a 7% increment in secondary OA relative
591 to H-BB. Worldwide studies (Jimenez et al., 2009; Mandariya et al., 2019; Sun et al., 2013) reported secondary
592 organic aerosol associated with a higher O/C ratio, and several studies reported that the O/C ratio positively
593 correlated to κ (Jimenez et al., 2009; Kim et al., 2020) as described in the earlier text. Furthermore, impacts of
594 5% decrement in ACI during H-HOA event concerning H-BB event possibly managed by 7% increment in AS
595 fraction. Overall, these relative changes in aerosol constituents worked to insignificant changes in κ during H-BB
596 and H-HOA periods. Nevertheless, H-BB and H-HOA events witnessed significant ($p < 0.05$) lower hygroscopicity
597 compared to a relatively cleaner atmosphere. The aerosol associated with relatively cleaner events was with a
598 higher inorganic-to-organic ratio. In addition, the aerosol in clean periods comprised a significantly higher fraction
599 of secondary organic aerosol, which could be the reason for the higher hygroscopicity associated with organic
600 aerosol compared to other events. Worldwide (Aiken et al., 2008; Cerully et al., 2015b; Chakraborty et al., 2016b;
601 Mandariya et al., 2019) studies have reported that organic aerosol loading inversely impacts the oxidation/aging
602 process of OA. Overall, all these were responsible for higher hygroscopicity in relatively cleaner periods.



603

604 Figure 9: Box plot showing variation in H-TDMA measured hygroscopic parameter of 200 nm size particles $\kappa_{\text{H-TDMA}}$
 605 ($\kappa_{200\text{nm}_90\%}$) in high biomass burning (H-BB), high-chloride (H-Cl), and high-hydrocarbon like organic aerosol (H-
 606 HOA) events. Different colors represent respective events in the plot. A bigger pie chart represents the overall average
 607 volume fractional contribution of various aerosol species indicated by color-coding. In addition, minor pie charts
 608 described the event average mass fractional contribution of different OA species in OA. Diffused ring color of the pie
 609 chart displays the respective event.

610 **4. Conclusions**

611 The present study investigated the temporal variation of hygroscopicity in aerosol particles of different sizes,
 612 namely Nucleation (20 nm), Aitken (50 nm), and Accumulation (150 and 200 nm) modes in Delhi during the
 613 winter period of February-March 2020. This research also highlighted variations in hygroscopicity, specifically
 614 in aerosols with higher chloride, biomass burning, and hydrocarbon-like organic components. Delhi, known as

615 one of the most polluted cities, often experiences high levels of chloride pollution during winter haze and fog
616 events. Consequently, this study reported the temporal variations in size-specific hygroscopic parameters ($\kappa_{H-TDMA_90\%}$) under sub-saturated conditions (90% RH) in Delhi for the first time. Furthermore, it presented the
617 hygroscopicity of nucleation and Aitken mode particles using HTDMA for the first time in India.
618

619 The observed $\kappa_{H-TDMA_90\%}$ values ranged from 0.00 to 0.11 (with an average of 0.03 ± 0.02) for 20 nm aerosol
620 particles, 0.05 to 0.22 (0.11 ± 0.03) for 50 nm particles, 0.05 to 0.30 (0.14 ± 0.04) for 100 nm particles, 0.05 to
621 0.41 (0.18 ± 0.06) for 150 nm particles, and 0.05 to 0.56 (0.22 ± 0.07) for 200 nm particles. The average
622 hygroscopicity parameter for the study period significantly increased with the size of the particles ($p<0.05$).
623 $\kappa_{20nm_90\%}$ and $\kappa_{50nm_90\%}$ displayed dynamic diurnal variations, while larger accumulation mode particles exhibited
624 a flatter diurnal pattern. This was attributed to the balancing positive and negative effects of changes in the volume
625 fraction of NH_4Cl and organic aerosol (OA) in the aerosol with increasing particle size. Interestingly, the variation
626 in $\kappa_{200nm_90\%}$ was primarily associated with fluctuations in NH_4Cl and OA, rather than $(\text{NH}_4)_2\text{SO}_4$.

627 Furthermore, pollution episodes were predominantly linked to local biomass burning and industrial and waste-
628 burning emissions in Delhi and nearby regions. The study primarily focused on highlighting the impacts of high
629 biomass burning (H-BB), high hydrocarbon-like OA (H-HOA), and high chloride emissions (H-Cl) on aerosol
630 hygroscopicity and compared them to cleaner periods. The H-Cl period exhibited significantly higher
631 hygroscopicity (0.35 ± 0.06) compared to H-BB (0.18 ± 0.04), H-HOA (0.17 ± 0.05), and the relatively cleaner
632 period (0.27 ± 0.07). However, H-BB and H-HOA showed no significant difference in hygroscopicity but
633 displayed lower hygroscopicity compared to cleaner periods. This could be attributed to lower organic aerosol
634 levels and a higher inorganic-to-organic aerosol ratio in the aerosol. The study also revealed that a 10% increase
635 in chloride aerosol (ammonium chloride) in the aerosol significantly enhanced hygroscopicity, leading to
636 approximately $3 \mu\text{g m}^{-3}$ higher aerosol liquid water content during high chloride events. This 10% enhancement
637 of a high-volume fraction of ammonium chloride in aerosol enhanced the aerosol hygroscopicity significantly
638 ($p<0.05$) by 0.0041. Furthermore, the research suggested that chloride emissions were a significant concern in
639 Delhi, enhancing aerosol hygroscopicity, promoting cloud formation during winter days, and contributing to fog
640 and haze in the region. High chloride levels in aerosols counteracted the negative impact of high OA loading on
641 cloud condensation nuclei (CCN) activity. Consequently, the results indicated that controlling open burning of
642 waste materials could help reduce haze and fog events in Delhi during the winter months.

643 **Supporting Information**

644 Supplementary pieces of information are mentioned in the supplementary file.

645 **Data availability.** Data can be accessed at the following repository:

646 <https://web.iitd.ac.in/~gazala/publications.html> (Mandariya et al., 2023).

647 **Author contributions**

648 AH, MMVH, NAB, and GH operated aerosol instrumentation and collection of data on-board in Delhi. KP
649 analysed the ACSM data. AKM, AH, and GH conceptualized the structure of the manuscript. AKM analysed,
650 evaluated H-TDMA data, and wrote the manuscript. AH analysed MPSS data. AKM, AH, KP, JSA, LHR, AW,
651 and GH internally reviewed the manuscript and helped to write the manuscript.

652 **Corresponding Author**

653 Gazala Habib (gazalahabib@civil.iitd.ac.in) and Alfred Wiedensohler (ali@tropos.de)

654 **Competing interests**

655 The authors declare that they have no conflict of interest.

656

657 **Acknowledgment**

658 The authors thankful to Dr. Martin Gysel, Aerosol Physics Group, Paul Scherrer Institute, Switzerland, for
659 providing TDMAinv toolkit for HTDMA data correction.

660 **REFERENCES**

661 Achtert, P., Birmili, W., Nowak, A., Wehner, B., Wiedensohler, A., Takegawa, N., Kondo, Y., Miyazaki, Y., Hu,
662 M. and Zhu, T.: Hygroscopic growth of tropospheric particle number size distributions over the North China Plain,
663 *J. Geophys. Res.*, 114(8), D00G07, doi:10.1029/2008JD010921, 2009.

664 Aiken, A. C., Decarlo, P. F., Kroll, J. H., Worsnop, D. R., Huffman, J. A., Docherty, K. S., Ulbrich, I. M., Mohr,
665 C., Kimmel, J. R., Sueper, D., Sun, Y., Zhang, Q., Trimborn, A., Northway, M., Ziemann, P. J., Canagaratna, M.
666 R., Onasch, T. B., Alfarra, M. R., Prevot, A. S. H., Dommen, J., Duplissy, J., Metzger, A., Baltensperger, U. and
667 Jimenez, J. L.: O/C and OM/OC ratios of primary, secondary, and ambient organic aerosols with high-resolution
668 time-of-flight aerosol mass spectrometry, *Environ. Sci. Technol.*, 42(12), 4478–4485, doi:10.1021/es703009q,
669 2008.

670 Albrecht, B. A.: Aerosols, Cloud Microphysics, and Fractional Cloudiness, *Science* (80-.), 245(4923), 1227–
671 1230, doi:10.1126/science.245.4923.1227, 1989.

672 Arub, Z., Bhandari, S., Gani, S., Apte, J. S., Hildebrandt Ruiz, L. and Habib, G.: Air mass physiochemical
673 characteristics over New Delhi: impacts on aerosol hygroscopicity and cloud condensation nuclei (CCN)
674 formation, *Atmos. Chem. Phys.*, 20(11), 6953–6971, doi:10.5194/acp-20-6953-2020, 2020.

675 Bhandari, S., Gani, S., Patel, K., Wang, D. S., Soni, P., Arub, Z., Habib, G., Apte, J. S. and Hildebrandt Ruiz, L.:
676 Sources and atmospheric dynamics of organic aerosol in New Delhi, India: insights from receptor modeling,
677 *Atmos. Chem. Phys.*, 20(2), 735–752, doi:10.5194/acp-20-735-2020, 2020.

678 Bhattu, D. and Tripathi, S. N.: CCN closure study: Effects of aerosol chemical composition and mixing state, *J. Geophys. Res.*, 120(2), 766–783, doi:10.1002/2014JD021978, 2015.

680 Bhattu, D., Tripathi, S. N. and Chakraborty, A.: Deriving aerosol hygroscopic mixing state from size-resolved
681 CCN activity and HR-ToF-AMS measurements, *Atmos. Environ.*, 142, 57–70,
682 doi:10.1016/j.atmosenv.2016.07.032, 2016.

683 Cerully, K. M., Bougiatioti, A., Hite, J. R., Guo, H., Xu, L., Ng, N. L., Weber, R. and Nenes, A.: On the link
684 between hygroscopicity, volatility, and oxidation state of ambient and water-soluble aerosols in the southeastern
685 United States, *Atmos. Chem. Phys.*, 15(15), 8679–8694, doi:10.5194/acp-15-8679-2015, 2015a.

686 Cerully, K. M., Bougiatioti, A., Hite, J. R., Guo, H., Xu, L., Ng, N. L., Weber, R. and Nenes, A.: On the link
687 between hygroscopicity, volatility, and oxidation state of ambient and water-soluble aerosols in the southeastern
688 United States, *Atmos. Chem. Phys.*, 15(15), 8679–8694, doi:10.5194/acp-15-8679-2015, 2015b.

689 Chakraborty, A., Gupta, T. and Tripathi, S. N.: Combined effects of organic aerosol loading and fog processing
690 on organic aerosols oxidation, composition, and evolution, *Sci. Total Environ.*, 573, 690–698,
691 doi:10.1016/j.scitotenv.2016.08.156, 2016a.

692 Chakraborty, A., Gupta, T. and Tripathi, S. N.: Combined effects of organic aerosol loading and fog processing
693 on organic aerosols oxidation, composition, and evolution, *Sci. Total Environ.*, 573, 690–698,
694 doi:10.1016/j.scitotenv.2016.08.156, 2016b.

695 Chen, Y., Wang, Y., Nenes, A., Wild, O., Song, S., Hu, D., Liu, D., He, J., Hildebrandt Ruiz, L., Apte, J. S.,
696 Gunthe, S. S. and Liu, P.: Ammonium Chloride Associated Aerosol Liquid Water Enhances Haze in Delhi, India,
697 *Environ. Sci. Technol.*, 56(11), 7163–7173, doi:10.1021/ACS.EST.2C00650, 2022.

698 Draxler, Roland R., Hess, G. D.: Description of the HYSPLIT_4 Modeling System, NOAA Technical Memo.
699 ERL ARL-224, (October 2004), 28 [online] Available from: <http://arlsun.arlhq.noaa.gov/documents/reports/arł-224.pdf> 5Cnhttp://www.ciecem.uhu.es/hysplitweb08/document/arł-224.pdf, 1997.

701 Duplissy, J., De Carlo, P. F., Dommen, J., Alfarra, M. R., Metzger, A., Barmpadimos, I., Prevot, A. S. H.,
702 Weingartner, E., Tritscher, T., Gysel, M., Aiken, A. C., Jimenez, J. L., Canagaratna, M. R., Worsnop, D. R.,
703 Collins, D. R., Tomlinson, J. and Baltensperger, U.: Relating hygroscopicity and composition of organic aerosol
704 particulate matter, *Atmos. Chem. Phys.*, 11(3), 1155–1165, doi:10.5194/acp-11-1155-2011, 2011.

705 Enroth, J., Mikkilä, J., Németh, Z., Kulmala, M. and Salma, I.: Wintertime hygroscopicity and volatility of
706 ambient urban aerosol particles, *Atmos. Chem. Phys.*, 18(7), 4533–4548, doi:10.5194/acp-18-4533-2018, 2018.

707 Ervens, B., Turpin, B. J. and Weber, R. J.: Secondary organic aerosol formation in cloud droplets and aqueous
708 particles (aqSOA): A review of laboratory, field and model studies, *Atmos. Chem. Phys.*, 11(21), 11069–11102,
709 doi:10.5194/acp-11-11069-2011, 2011.

710 Fan, X., Liu, J., Zhang, F., Chen, L., Collins, D., Xu, W., Jin, X., Ren, J., Wang, Y., Wu, H., Li, S., Sun, Y. and
711 Li, Z.: Contrasting size-resolved hygroscopicity of fine particles derived by HTDMA and HR-ToF-AMS
712 measurements between summer and winter in Beijing: the impacts of aerosol aging and local emissions, *Atmos.*
713 *Chem. Phys.*, 20(2), 915–929, doi:10.5194/acp-20-915-2020, 2020.

714 Fountoukis, C. and Nenes, A.: ISORROPIAII: A computationally efficient thermodynamic equilibrium model for
715 K⁺-Ca²⁺-Mg²⁺-NH⁴⁺-Na⁺-SO₄²⁻-NO₃⁻-Cl⁻-H₂O aerosols, *Atmos. Chem. Phys.*, 7(17), 4639–4659,
716 doi:10.5194/acp-7-4639-2007, 2007.

717 Gani, S., Bhandari, S., Seraj, S., Wang, D. S., Patel, K., Soni, P., Arub, Z., Habib, G., Hildebrandt Ruiz, L. and
718 Apte, J. S.: Submicron aerosol composition in the world's most polluted megacity: the Delhi Aerosol Supersite
719 study, *Atmos. Chem. Phys.*, 19(10), 6843–6859, doi:10.5194/acp-19-6843-2019, 2019.

720 Gunthe, S. S., Rose, D., Su, H., Garland, R. M., Achtert, P., Nowak, A., Wiedensohler, A., Kuwata, M., Takegawa, N., Kondo, Y., Hu, M., Shao, M., Zhu, T., Andreae, M. O. and Pöschl, U.: Cloud condensation nuclei (CCN) from fresh and aged air pollution in the megacity region of Beijing, *Atmos. Chem. Phys.*, 11(21), 11023–11039, doi:10.5194/acp-11-11023-2011, 2011.

724 Gunthe, S. S., Liu, P., Panda, U., Raj, S. S., Sharma, A., Darbyshire, E., Reyes-Villegas, E., Allan, J., Chen, Y., Wang, X., Song, S., Pöhlker, M. L., Shi, L., Wang, Y., Kommula, S. M., Liu, T., Ravikrishna, R., McFiggans, G., Mickley, L. J., Martin, S. T., Pöschl, U., Andreae, M. O. and Coe, H.: Enhanced aerosol particle growth sustained by high continental chlorine emission in India, *Nat. Geosci.*, 14(2), 77–84, doi:10.1038/s41561-020-00677-x, 2021.

729 Gupta, T. and Mandariya, A.: Sources of submicron aerosol during fog-dominated wintertime at Kanpur, *Environ. Sci. Pollut. Res.*, 20(8), doi:10.1007/s11356-013-1580-6, 2013.

731 Gysel, M., Crosier, J., Topping, D. O., Whitehead, J. D., Bower, K. N., Cubison, M. J., Williams, P. I., Flynn, M. J., McFiggans, G. B. and Coe, H.: Closure study between chemical composition and hygroscopic growth of aerosol particles during TORCH2, *Atmos. Chem. Phys.*, 7(24), 6131–6144, doi:10.5194/acp-7-6131-2007, 2007.

734 Gysel, M., McFiggans, G. B. and Coe, H.: Inversion of tandem differential mobility analyser (TDMA) measurements, *J. Aerosol Sci.*, 40(2), 134–151, doi:10.1016/j.jaerosci.2008.07.013, 2009.

736 Hallquist, M., Wenger, J. C., Baltensperger, U., Rudich, Y., Simpson, D., Claeys, M., Dommen, J., Donahue, N. M., George, C., Goldstein, A. H., Hamilton, J. F., Herrmann, H., Hoffmann, T., Linuma, Y., Jang, M., Jenkin, M. E., Jimenez, J. L., Kiendler-Scharr, A., Maenhaut, W., McFiggans, G., Mentel, T. F., Monod, A., Pfeifert, A. S. H., Seinfeld, J. H., Surratt, J. D., Szmigielski, R. and Wildt, J.: The formation, properties and impact of secondary organic aerosol: current and emerging issues, *Atmos. Chem. Phys.*, 9(November 2008), 5155–5236, 2009.

741 Hong, J., Häkkinen, S. A. K., Paramonov, M., Äijälä, M., Hakala, J., Nieminen, T., Mikkilä, J., Prisle, N. L., Kulmala, M., Riipinen, I., Bilde, M., Kerminen, V. M. and Petäjä, T.: Hygroscopicity, CCN and volatility properties of submicron atmospheric aerosol in a boreal forest environment during the summer of 2010, *Atmos. Chem. Phys.*, 14(9), 4733–4748, doi:10.5194/acp-14-4733-2014, 2014.

745 Hong, J., Kim, J., Nieminen, T., Duplissy, J., Ehn, M., Äijälä, M., Hao, L. Q., Nie, W., Sarnela, N., Prisle, N. L., Kulmala, M., Virtanen, A., Petäjä, T. and Kerminen, V. M.: Relating the hygroscopic properties of submicron aerosol to both gas- and particle-phase chemical composition in a boreal forest environment, *Atmos. Chem. Phys.*, 15(20), 11999–12009, doi:10.5194/acp-15-11999-2015, 2015.

749 Hong, J., Xu, H., Tan, H., Yin, C., Hao, L., Li, F., Cai, M., Deng, X., Wang, N., Su, H., Cheng, Y., Wang, L., Petäjä, T. and Kerminen, V. M.: Mixing state and particle hygroscopicity of organic-dominated aerosols over the Pearl River Delta region in China, *Atmos. Chem. Phys.*, 18(19), 14079–14094, doi:10.5194/acp-18-14079-2018, 2018.

753 Hu, D., Chen, J., Ye, X., Li, L. and Yang, X.: Hygroscopicity and evaporation of ammonium chloride and ammonium nitrate: Relative humidity and size effects on the growth factor, *Atmos. Environ.*, 45(14), 2349–2355, doi:10.1016/j.atmosenv.2011.02.024, 2011.

756 Jimenez, J. L., Canagaratna, M. R., Donahue, N. M., Prevot, A. S. H., Zhang, Q., Kroll, J. H., DeCarlo, P. F., Allan, J. D., Coe, H., Ng, N. L., Aiken, A. C., Docherty, K. S., Ulbrich, I. M., Grieshop, A. P., Robinson, A. L., Duplissy, J., Smith, J. D., Wilson, K. R., Lanz, V. A., Hueglin, C., Sun, Y. L., Tian, J., Laaksonen, A., Raatikainen, T., Rautiainen, J., Vaattovaara, P., Ehn, M., Kulmala, M., Tomlinson, J. M., Collins, D. R., Cubison, M. J., Dunlea, E. J., Huffman, J. A., Onasch, T. B., Alfarra, M. R., Williams, P. I., Bower, K., Kondo, Y., Schneider, J., Drewnick, F., Borrmann, S., Weimer, S., Demerjian, K., Salcedo, D., Cottrell, L., Griffin, R., Takami, A., Miyoshi, T., Hatakeyama, S., Shimono, A., Sun, J. Y., Zhang, Y. M., Dzepina, K., Kimmel, J. R., Sueper, D., Jayne, J. T., Herndon, S. C., Trimborn, A. M., Williams, L. R., Wood, E. C., Middlebrook, A. M., Kolb, C. E., Baltensperger, U. and Worsnop, D. R.: Evolution of organic aerosols in the atmosphere, *Science* (80-), 326(5959), 1525–1529, doi:10.1126/science.1180353, 2009.

766 Kawana, K., Nakayama, T. and Mochida, M.: Hygroscopicity and CCN activity of atmospheric aerosol particles and their relation to organics: Characteristics of urban aerosols in Nagoya, Japan, *J. Geophys. Res. Atmos.*, 121(8), 4100–4121, doi:10.1002/2015JD023213, 2016.

769 Kecorius, S., Vogl, T., Paasonen, P., Lampilahti, J., Rothenberg, D., Wex, H., Zeppenfeld, S., Van Pinxteren, M.,
 770 Hartmann, M., Henning, S., Gong, X., Welti, A., Kulmala, M., Stratmann, F., Herrmann, H. and Wiedensohler,
 771 A.: New particle formation and its effect on cloud condensation nuclei abundance in the summer Arctic: a case
 772 study in the Fram Strait and Barents Sea, *Atmos. Chem. Phys.*, 19, 14339–14364, doi:10.5194/acp-19-14339-2019,
 773 2019.

774 Kim, N., Park, M., Yum, S. S., Park, J. S., Song, I. H., Shin, H. J., Ahn, J. Y., Kwak, K. H., Kim, H., Bae, G. N.
 775 and Lee, G.: Hygroscopic properties of urban aerosols and their cloud condensation nuclei activities measured in
 776 Seoul during the MAPS-Seoul campaign, *Atmos. Environ.*, 153, 217–232, doi:10.1016/j.atmosenv.2017.01.034,
 777 2017.

778 Kim, N., Yum, S. S., Park, M., Park, J. S., Shin, H. J. and Ahn, J. Y.: Hygroscopicity of urban aerosols and its
 779 link to size-resolved chemical composition during spring and summer in Seoul, Korea, *Atmos. Chem. Phys.*,
 780 20(19), 11245–11262, doi:10.5194/acp-20-11245-2020, 2020.

781 Kitamori, Y., Mochida, M. and Kawamura, K.: Assessment of the aerosol water content in urban atmospheric
 782 particles by the hygroscopic growth measurements in Sapporo, Japan, *Atmos. Environ.*, 43(21), 3416–3423,
 783 doi:10.1016/j.atmosenv.2009.03.037, 2009.

784 Kroll, J. H., Donahue, N. M., Jimenez, J. L., Kessler, S. H., Canagaratna, M. R., Wilson, K. R., Altieri, K. E.,
 785 Mazzoleni, L. R., Wozniak, A. S., Bluhm, H., Mysak, E. R., Smith, J. D., Kolb, C. E. and Worsnop, D. R.: Carbon
 786 oxidation state as a metric for describing the chemistry of atmospheric organic aerosol, *Nat. Chem.*, 3(2), 133–
 787 139, doi:10.1038/nchem.948, 2011.

788 Li, H., Wang, Q., Shao, M., Wang, J., Wang, C., Sun, Y., Qian, X., Wu, H., Yang, M. and Li, F.: Fractionation of
 789 airborne particulate-bound elements in haze-fog episode and associated health risks in a megacity of southeast
 790 China, *Environ. Pollut.*, 208, 655–662, doi:10.1016/j.envpol.2015.10.042, 2016.

791 Liu, J., Horowitz, L. W., Fan, S., Carlton, A. G. and Levy, H.: Global in-cloud production of secondary organic
 792 aerosols: Implementation of a detailed chemical mechanism in the GFDL atmospheric model AM3, *J. Geophys.
 793 Res. Atmos.*, 117(D15), n/a-n/a, doi:10.1029/2012JD017838, 2012.

794 Lohmann, U. and Feichter, J.: Global indirect aerosol effects: a review, *Atmos. Chem. Phys.*, 5(3), 715–737,
 795 doi:10.5194/acp-5-715-2005, 2005.

796 Mandariya, A. K., Gupta, T. and Tripathi, S. N.: Effect of aqueous-phase processing on the formation and
 797 evolution of organic aerosol (OA) under different stages of fog life cycles, *Atmos. Environ.*, 206(November 2018),
 798 60–71, doi:10.1016/j.atmosenv.2019.02.047, 2019.

799 Mandariya, A. K., Tripathi, S. N., Gupta, T. and Mishra, G.: Wintertime hygroscopic growth factors (HGFs) of
 800 accumulation mode particles and their linkage to chemical composition in a heavily polluted urban atmosphere of
 801 Kanpur at the Centre of IGP, India: Impact of ambient relative humidity, *Sci. Total Environ.*, 704, 135363,
 802 doi:10.1016/j.scitotenv.2019.135363, 2020a.

803 Mandariya, A. K., Tripathi, S. N., Gupta, T. and Mishra, G.: Wintertime hygroscopic growth factors (HGFs) of
 804 accumulation mode particles and their linkage to chemical composition in a heavily polluted urban atmosphere of
 805 Kanpur at the Centre of IGP, India: Impact of ambient relative humidity, *Sci. Total Environ.*, 704,
 806 doi:10.1016/j.scitotenv.2019.135363, 2020b.

807 Massling, A., Leinert, S., Wiedensohler, A. and Covert, D.: Hygroscopic growth of sub-micrometer and one-
 808 micrometer aerosol particles measured during ACE-Asia, *Atmos. Chem. Phys.*, 7, 3249–3259 [online] Available
 809 from: www.atmos-chem-phys.net/7/3249/2007/ (Accessed 30 October 2022), 2007.

810 Maßling, A., Wiedensohler, A., Busch, B., Neusüß, C., Neusüß, N., Quinn, P., Bates, T. and Covert, D.:
 811 Atmospheric Chemistry and Physics Hygroscopic properties of different aerosol types over the Atlantic and Indian
 812 Oceans, *Atmos. Chem. Phys.*, 3, 1377–1397 [online] Available from: www.atmos-chem-phys.org/acp/3/1377/
 813 (Accessed 30 October 2022), 2003.

814 Massoli, P., Lambe, A. T., Ahern, A. T., Williams, L. R., Ehn, M., Mikkilä, J., Canagaratna, M. R., Brune, W. H.,
 815 Onasch, T. B., Jayne, J. T., Petäjä, T., Kulmala, M., Laaksonen, A., Kolb, C. E., Davidovits, P. and Worsnop, D.

816 R.: Relationship between aerosol oxidation level and hygroscopic properties of laboratory generated secondary
817 organic aerosol (SOA) particles, *Geophys. Res. Lett.*, 37(24), 1–5, doi:10.1029/2010GL045258, 2010.

818 McFiggans, G., Artaxo, P., Baltensperger, U., Coe, H., Facchini, M. C., Feingold, G., Fuzzi, S., Gysel, M.,
819 Laaksonen, A., Lohmann, U., Mentel, T. F., Murphy, D. M., O'Dowd, C. D., Snider, J. R. and Weingartner, E.:
820 The effect of physical and chemical aerosol properties on warm cloud droplet activation, *Atmos. Chem. Phys.*,
821 6(9), 2593–2649, doi:10.5194/acp-6-2593-2006, 2006.

822 McNeill, V. F.: Aqueous organic chemistry in the atmosphere: Sources and chemical processing of organic
823 aerosols, *Environ. Sci. Technol.*, 49(3), 1237–1244, doi:10.1021/es5043707, 2015.

824 Mei, F., Setyan, A., Zhang, Q. and Wang, J.: CCN activity of organic aerosols observed downwind of urban
825 emissions during CARES, *Atmos. Chem. Phys.*, 13(24), 12155–12169, doi:10.5194/acp-13-12155-2013, 2013.

826 Ng, N. L., Herndon, S. C., Trimborn, A., Canagaratna, M. R., Croteau, P. L., Onasch, T. B., Sueper, D., Worsnop,
827 D. R., Zhang, Q., Sun, Y. L. and Jayne, J. T.: An Aerosol Chemical Speciation Monitor (ACSM) for routine
828 monitoring of the composition and mass concentrations of ambient aerosol, *Aerosol Sci. Technol.*, 45(7), 780–
829 794, doi:10.1080/02786826.2011.560211, 2011.

830 Ogawa, S., Setoguchi, Y., Kawana, K., Nakayama, T., Ikeda, Y., Sawada, Y., Matsumi, Y. and Mochida, M.:
831 Hygroscopicity of aerosol particles and CCN activity of nearly hydrophobic particles in the urban atmosphere
832 over Japan during summer, *J. Geophys. Res.*, 121(12), 7215–7234, doi:10.1002/2015JD024636, 2016.

833 Petit, J. E., Favez, O., Albinet, A. and Canonaco, F.: A user-friendly tool for comprehensive evaluation of the
834 geographical origins of atmospheric pollution: Wind and trajectory analyses, *Environ. Model. Softw.*, 88, 183–
835 187, doi:10.1016/j.envsoft.2016.11.022, 2017.

836 Petters, M. D. and Kreidenweis, S. M.: A single parameter representation of hygroscopic growth and cloud
837 condensation nucleus activity, *Atmos. Chem. Phys. Atmos. Chem. Phys.*, 7, 1961–1971, doi:10.5194/acp-7-1961-
838 2007, 2007.

839 Prakash, J., Lohia, T., Mandariya, A. K., Habib, G., Gupta, T. and Gupta, S. K.: Chemical characterization and
840 quantitativ e assessment of source-specific health risk of trace metals in PM1.0 at a road site of Delhi, India,
841 *Environ. Sci. Pollut. Res.*, 25(9), 8747–8764, doi:10.1007/s11356-017-1174-9, 2018.

842 Pringle, K. J., Tost, H., Pozzer, A., Pöschl, U. and Lelieveld, J.: Global distribution of the effective aerosol
843 hygroscopicity parameter for CCN activation, *Atmos. Chem. Phys.*, 10(12), 5241–5255, doi:10.5194/acp-10-
844 5241-2010, 2010.

845 Rai, P., Furger, M., El Haddad, I., Kumar, V., Wang, L., Singh, A., Dixit, K., Bhattu, D., Petit, J.-E., Ganguly, D.,
846 Rastogi, N., Baltensperger, U., Tripathi, S. N., Slowik, J. G. and Prévôt, A. S. H.: Real-time measurement and
847 source apportionment of elements in Delhi's atmosphere, *Sci. Total Environ.*, 742, 140332,
848 doi:10.1016/j.scitotenv.2020.140332, 2020.

849 Randall, D A; Wood, R A; Bony, S; Colman, R; Fichefet, T; Fyfe, J; Kattsov, V; Pitman, A; Shukla, J; Srinivasan,
850 J; Stouffer, R J; Sumi, A; Taylor, K. E.: Climate Models and Their Application, *Clim. Chang.* 2007 Phys. Sci.
851 Basis. Contrib. Work. Gr. I to Fourth Assess. Rep. Intergov. Panel Clim. Chang. Ed. by S. Solomon al., Cambridge
852 Univ. Press. Cambridge, U. K., New York., Chapter 8(United Kingdom: N. p., p.2007. Web.), 590–662,
853 doi:<http://www.ipcc.ch/pdf/assessment-report/ar4/wg1/ar4-wg1-chapter8.pdf>, 2007.

854 Richard, A., Gianini, M. F. D., Mohr, C., Furger, M., Bukowiecki, N. and Minguill, M. C.: and Physics Source
855 apportionment of size and time resolved trace elements and organic aerosols from an urban courtyard site in
856 Switzerland , 8945–8963, doi:10.5194/acp-11-8945-2011, 2011.

857 Seinfeld, J. H. and Pandis, S. N.: Atmospheric cemistry and physics: From air pollution to climate change, Second
858 edi., John Wiley & Sons, Inc., 2006.

859 Shukla, A. K., Lalchandani, V., Bhattu, D., Dave, J. S., Rai, P., Thamban, N. M., Mishra, S., Gaddamidi, S.,
860 Tripathi, N., Vats, P., Rastogi, N., Sahu, L., Ganguly, D., Kumar, M., Singh, V., Gargava, P. and Tripathi, S. N.:
861 Real-time quantification and source apportionment of fine particulate matter including organics and elements in

862 Delhi during summertime, *Atmos. Environ.*, 261, 118598, doi:10.1016/J.ATMOSENV.2021.118598, 2021.

863 Sjogren, S., Gysel, M., Weingartner, E., Baltensperger, U., Cubison, M. J. and Coe, H.: Hygroscopic growth and
864 water uptake kinetics of two-phase aerosol particles consisting of ammonium sulfate , adipic and humic acid
865 mixtures , 38, 157–171, doi:10.1016/j.jaerosci.2006.11.005, 2007.

866 Sjogren, S., Gysel, M., Weingartner, E., Alfarra, M. R., Duplissy, J., Cozic, J., Crosier, J. and Coe, and U. B.:
867 Hygroscopicity of the submicrometer aerosol at the high-alpine site Jungfraujoch, 3580m a.s.l., Switzerland ,
868 7231–7249, doi:10.5194/acp-12-7231-2012, 2012.

869 Stokes, R. H. and Robinson, R. A.: Interactions in Aqueous Nonelectrolyte Solutions. I. Solute-Solvent Equilibria,
870 *J. Phys. Chem.*, 70(7), 2126–2131, doi:10.1021/j100879a010, 1966.

871 Su, H., Rose, D., Cheng, Y. F., Gunthe, S. S., Massling, A., Stock, M., Wiedensohler, A., Andreae, M. O. and
872 Pöschl, U.: Hygroscopicity distribution concept for measurement data analysis and modeling of aerosol particle
873 mixing state with regard to hygroscopic growth and CCN activation, *Atmos. Chem. Phys.*, 10, 7489–7503,
874 doi:10.5194/acp-10-7489-2010, 2010.

875 Sun, Y., Wang, Z., Fu, P., Jiang, Q., Yang, T., Li, J. and Ge, X.: The impact of relative humidity on aerosol
876 composition and evolution processes during wintertime in Beijing , China, *Atmos. Environ.*, 77, 927–934,
877 doi:10.1016/j.atmosenv.2013.06.019, 2013.

878 Sun, Y., Du, W., Fu, P., Wang, Q., Li, J., Ge, X., Zhang, Q., Zhu, C., Ren, L., Xu, W., Zhao, J., Han, T., Worsnop,
879 D. R. and Wang, Z.: Primary and secondary aerosols in Beijing in winter: Sources, variations and processes,
880 *Atmos. Chem. Phys.*, 16(13), 8309–8329, doi:10.5194/acp-16-8309-2016, 2016.

881 Swietlicki, E., Hansson, H. C., Hämeri, K., Svenningsson, B., Massling, A., McFiggans, G., McMurry, P. H.,
882 Petäjä, T., Tunved, P., Gysel, M., Topping, D., Weingartner, E., Baltensperger, U., Rissler, J., Wiedensohler, A.
883 and Kulmala, M.: Hygroscopic properties of submicrometer atmospheric aerosol particles measured with H-
884 TDMA instruments in various environments—a review, *Tellus B Chem. Phys. Meteorol.*, 60(3), 432–469,
885 doi:10.1111/j.1600-0889.2008.00350.x, 2008.

886 Tang, I. N. and Munkelwitz, H. R.: Water activities, densities, and refractive indices of aqueous sulfates and
887 sodium nitrate droplets of atmospheric importance, *J. Geophys. Res.*, 99(D9), 18801, doi:10.1029/94JD01345,
888 1994.

889 Tobler, A., Bhattu, D., Canonaco, F., Lalchandani, V., Shukla, A., Thamban, N. M., Mishra, S., Srivastava, A. K.,
890 Bisht, D. S., Tiwari, S., Singh, S., Močnik, G., Baltensperger, U., Tripathi, S. N., Slowik, J. G. and Prévôt, A. S.
891 H.: Chemical characterization of PM2.5 and source apportionment of organic aerosol in New Delhi, India, *Sci.
892 Total Environ.*, 745, 140924, doi:10.1016/J.SCITOTENV.2020.140924, 2020.

893 Topping, D. O. and McFiggans, G.: Tight coupling of particle size, number and composition in atmospheric cloud
894 droplet activation, *Atmos. Chem. Phys.*, 12(7), 3253–3260, doi:10.5194/acp-12-3253-2012, 2012.

895 Tritscher, T., Jurnyi, Z., Martin, M., Chirico, R., Gysel, M., Heringa, M. F., Decarlo, P. F., Sierau, B., Prévôt, A.
896 S. H., Weingartner, E. and Baltensperger, U.: Changes of hygroscopicity and morphology during ageing of diesel
897 soot, *Environ. Res. Lett.*, 6(3), doi:10.1088/1748-9326/6/3/034026, 2011.

898 Wang, X., Shen, X. J., Sun, J. Y., Zhang, X. Y., Wang, Y. Q., Zhang, Y. M., Wang, P., Xia, C., Qi, X. F. and
899 Zhong, J. T.: Size-resolved hygroscopic behavior of atmospheric aerosols during heavy aerosol pollution episodes
900 in Beijing in December 2016, , 194(September), 188–197, doi:10.1016/j.atmosenv.2018.09.041, 2018a.

901 Wang, Y., Wu, Z., Ma, N., Wu, Y., Zeng, L., Zhao, C. and Wiedensohler, A.: Statistical analysis and
902 parameterization of the hygroscopic growth of the sub-micrometer urban background aerosol in Beijing, *Atmos.
903 Environ.*, 175(December 2017), 184–191, doi:10.1016/j.atmosenv.2017.12.003, 2018b.

904 Wester, P., Mishra, A., Mukherji, A., Shrestha, A. B. and Change, C.: The Hindu Kush Himalaya Assessment,
905 edited by P. Wester, A. Mishra, A. Mukherji, and A. B. Shrestha, Springer International Publishing, Cham., 2019.

906 Wu, Z. J., Poulain, L., Henning, S., Dieckmann, K., Birmili, W., Merkel, M., van Pinxteren, D., Spindler, G.,

907 Müller, K., Stratmann, F., Herrmann, H. and Wiedensohler, A.: Relating particle hygroscopicity and CCN activity
908 to chemical composition during the HCCT-2010 field campaign, *Atmos. Chem. Phys.*, 13(16), 7983–7996,
909 doi:10.5194/acp-13-7983-2013, 2013a.

910 Wu, Z. J., Poulain, L., Henning, S., Dieckmann, K., Birmili, W., Merkel, M., Van Pinxteren, D., Spindler, G.,
911 Stratmann, F., Herrmann, H. and Wiedensohler, A.: Sciences ess Atmospheric Chemistry and Physics Climate of
912 the Past Geoscientific Instrumentation Methods and Data Systems Relating particle hygroscopicity and CCN
913 activity to chemical composition during the HCCT-2010 field campaign, *Atmos. Chem. Phys.*, 13, 7983–7996,
914 doi:10.5194/acp-13-7983-2013, 2013b.

915 Wu, Z. J., Zheng, J., Shang, D. J., Du, Z. F., Wu, Y. S., Zeng, L. M., Wiedensohler, A. and Hu, M.: Particle
916 hygroscopicity and its link to chemical composition in the urban atmosphere of Beijing , China , during
917 summertime, , 1123–1138, doi:10.5194/acp-16-1123-2016, 2016.

918 Yeung, M. C., Lee, B. P., Li, Y. J. and Chan, C. K.: Simultaneous HTDMA and HR-ToF-AMS measurements at
919 the HKUST supersite in Hong Kong in 2011, *J. Geophys. Res.*, 119(16), 9864–9883, doi:10.1002/2013JD021146,
920 2014.

921 Zhang, Q., Jimenez, J. L., Worsnop, D. R. and Canagaratna, M.: A Case Study of Urban Particle Acidity and Its
922 Influence on Secondary Organic Aerosol, *Environ. Sci. Technol.*, 41(9), 3213–3219, doi:10.1021/es061812j,
923 2007.

924 Zhang, S. L., Ma, N., Kecorius, S., Wang, P. C., Hu, M., Wang, Z. B., Größ, J., Wu, Z. J. and Wiedensohler, A.:
925 Mixing state of atmospheric particles over the North China Plain, *Atmos. Environ.*, 125, 152–164,
926 doi:10.1016/J.ATMOSENV.2015.10.053, 2016.

927 Zhang, Y., Tang, L., Yu, H., Wang, Z., Sun, Y., Qin, W., Chen, W., Chen, C., Ding, A., Wu, J., Ge, S. and Chen,
928 C.: Chemical composition , sources and evolution processes of aerosol at an urban site in Yangtze River Delta ,
929 China during wintertime, *Atmos. Environ.*, 123, 339–349, doi:10.1016/j.atmosenv.2015.08.017, 2015.

930 Zhao, P., Du, X., Su, J., Ding, J. and Dong, Q.: Aerosol hygroscopicity based on size-resolved chemical
931 compositions in Beijing, *Sci. Total Environ.*, 716, 137074, doi:10.1016/J.SCITOTENV.2020.137074, 2020.

932